Department of Electrical Engineering and Automation

Design of the Contact Metallizations for Gold-Tin Eutectic Solder-A Thermodynamic-Kinetic Analysis

Hongqun Dong

Aalto University

DOCTORAL DISSERTATIONS

Aalto University publication series
DOCTORAL DISSERTATIONS 176/2016

Design of the Contact Metallizations for Gold-Tin Eutectic Solder-A Thermodynamic-Kinetic Analysis

Hongqun Dong

A doctoral dissertation completed for the degree of Doctor of Science (Technology) to be defended, with the permission of the Aalto University School of Electrical Engineering, at a public examination held at the lecture hall AS1 in TUAS building on 30 September 2016 at 12:00 pm.

Aalto University
School of Electrical Engineering
Department of Electrical Engineering and Automation
Electrical integration and reliability

Supervising professor
Mervi Paulasto-Kröckel, Aalto University, Finland

Thesis advisor
Vesa Vuorinen, Aalto University, Finland

Preliminary examiners
Prof. Aleš Kroupa, Institute of Physics of Materials, Academy of Science of the Czech Republic

Prof. C. Robert Kao, National Taiwan University, Taiwan

Opponents
Prof. Aleš Kroupa, Institute of Physics of Materials, Academy of Science of the Czech Republic, Czech Republic

Prof. Heli Jantunen, University of Oulu, Finland

Aalto University publication series
DOCTORAL DISSERTATIONS 176/2016

ISBN 978-952-60-6996-8 (printed)
ISBN 978-952-60-6995-1 (pdf)
ISSN-L 1799-4934
ISSN 1799-4934 (printed)
ISSN 1799-4942 (pdf)
http://urn.fi/URN:ISBN:978-952-60-6995-1

Unigrafia Oy
Helsinki 2016

Finland

Author
Hongqun Dong

Name of the doctoral dissertation
Design of the Contact Metallizations for Gold-Tin Eutectic Solder-A Thermodynamic-Kinetic Analysis

Publisher School of Electrical Engineering

Unit Department of Electrical Engineering and Automation

Series Aalto University publication series DOCTORAL DISSERTATIONS 176/2016

Field of research Electronics Production Technology

Manuscript submitted 30 August 2016 **Date of the defence** 30 September 2016

Permission to publish granted (date) 2 August 2016 **Language** English

☐ **Monograph** ☒ **Article dissertation** ☐ **Essay dissertation**

Abstract

This dissertation focuses on the design of reliable interconnections using Au-20wt.%Sn solder with the assistance of thermodynamic calculations. In this work, three commonly encountered contact metallizations, namely Ni, Cu, and Pt, have been selected. In order to assess the reliability of the Au-20wt.%Sn|X (X=Ni, Cu and Pt) interconnections from the metallurgical viewpoint, firstly, the phase diagrams of the Au-Sn-X ternary systems have been thermodynamically established with the Calphad method. Secondly, the diffusion couple method was employed to study the interfacial reactions experimentally. The microstructures of the as-soldered and subsequently aged Au-20wt.%Sn|X interconnections were characterized by means of scanning electron microscopy equipped with energy-dispersive X-ray spectroscopy (EDX) and scanning transmission electron microscopy with EDX. The observed interfacial reaction phenomena have been rationalized by combining the experimental results with the thermodynamic considerations. Emphasis has also been placed on collecting the mechanical properties of the IMCs formed at the solder/Cu and Ni interfaces since these values are essential for evaluating the reliability of the interconnections.

The results in this dissertation show that Au-20wt.%Sn|Pt was more thermally stable than Au-20wt.%Sn|Ni and Au-20wt.%Sn|Cu when these as-soldered reaction couples were subsequently aged at 150 °C for a long-term. When a short bonding time is employed, Pt contact metallization is superior to the Ni and Cu contact metallizations for the Au-20wt.%Sn solder.

Keywords Contact metallization (Ni, Cu, Pt), Au-20wt.%Sn solder, Calphad, microstructural characterization, interfacial reaction, mechanical properties

ISBN (printed) 978-952-60-6996-8 **ISBN (pdf)** 978-952-60-6995-1

ISSN-L 1799-4934 **ISSN (printed)** 1799-4934 **ISSN (pdf)** 1799-4942

Location of publisher Helsinki **Location of printing** Helsinki **Year** 2016

Pages 130 **urn** http://urn.fi/URN:ISBN:978-952-60-6995-1

Acknowledgements

This work has been conducted in the Electronics Integration and Reliability unit under the Department of Electrical Engineering and Automation at Aalto University. The work was financially supported by a four year doctoral program (GETA) and two projects ('Real Metal', and 'LabIV-MEMSII'). The projects were funded by the Academy of Finland, EU Eniac, the Finnish Funding Agency for Technology and Innovation (TEKES), Okmetic and Murata Electronics Oy.

I would like to express my sincere gratitude to my supervisor Professor Mervi Paulasto-Kröckel for her continuous support for my research. I have been extremely fortunate to have a supervisor who gave me the freedom to explore on my own. I appreciate all her contributions to make my doctoral stage productive. Without her patience, insightful comments and motivation, this dissertation would not have been possible.

My sincere thanks also go to my instructor, Dr. Vesa Vuorinen, for his guidance, suggestions and willingness to enter into insightful discussion at any time. I am deeply grateful to my former instructor, Prof. Tomi Laurila, for the help he gave me. The extensive discussions we have had have inspired me greatly. I am also thankful to them for carefully reading and commenting on countless revisions of my manuscripts.

I am also indebted to my past and present group members that I have had the pleasure to work with. I would particularly thank Prof. Xiaoma Tao, Dr. Xuwen Liu and Mikael Broas for conducting the first-principle calculations, nanoindentation tests and STEM-EDX analysis. I am also very grateful to Ms. Pirjo Kontio, Ms. Leena Väisänen, Ms. Marja Leppäharju and Mr. Esa Kurhinen for their time and kind assistance. I thank my friends in Finland for the useful tips they have given me along the way and the great times that we have shared.

Finally, I would like to thank my family. I thank my parents, Shujun and Shumin, for their faith in me and allowing me to be as ambitious as I wanted. I thank also my younger sister, Min, for her understanding and support. I dedicate this dissertation to the memory of my grandfather Kuixing Dong, whose role in my life was, and remains, immense. The last words of acknowledgement I have saved for my dear husband and our son who have made my life even better.

Espoo, May, 2016
Hongqun Dong

Contents

List of Abbreviations and Symbols

AES	auger electron spectroscopy
Calphad	CALculation of the PHAse Diagrams
CTE	coefficient of thermal expansion
EDX	energy-dispersive X-ray spectroscopy
EPMA	electron probe micro-analyzer
FIB	focused iron beam
HAADF	high-angle annular dark-field detector
IMCs	intermetallic compounds
MEMS	micro-electro-mechanical system
RBS	Rutherford backscattering spectrometry
SAM	scanning acoustic microscopy
SEM	scanning electron microscopy
SER	standard element reference
SGTE	scientific group thermo-data Europe
STEM	scanning transmission electron microscopy
TEM	transmission electron microscopy
TFP	thin film packaging
TLP	transient liquid bonding
WB	wafer bonding

XRD	X-ray diffraction
a_i	the activity of component i in the solution
C	the number of components
F	the number of independent variables, or called degrees of freedom
G	the total Gibbs energy
G_{ex}^{ϕ}	the excess Gibbs energy
G_{mag}^{ϕ}	the magnetic contribution to the total Gibbs energy
G_{ref}^{ϕ}	the contribution from mechanical mixing of constituents
G_{P}^{ϕ}	the contribution from pressure-dependent properties
G_{surf}^{ϕ}	the contribution of surface energy
$^{\circ}G_i$	the molar free energy of pure component i
$\overline{G_i}$	the partial molar Gibbs energy of component i
L_{ij}^{i}	the binary interaction parameters
L_{ijk}^{i}	the ternary interaction parameters
N_i	the number of moles of components i
p	the number of phases in equilibrium
P	Pressure
P_i	the products
p_i	number of moles of the products
R	the gas constant
R_i	the reactants
r_i	the number of moles of the reactants
S	the entropy of the system

${}^{cnf}S^{\phi}$	the configurational entropy of the phase
T	Temperature in Kevin
U	the internal energy the system
V	the volume of the system
X	X= Ni, Cu and Pt
x_i	the molar fraction of components
ΔG	the change in the Gibbs energy for a chemical reaction
μ_i	the chemical potential of component i
$^{\circ}\mu_i$	the chemical potential of component i in a given standard state

List of Publications

This doctoral dissertation consists of a summary and of the following publications which are referred to in the text by their numerals

1. Dong Hongqun, Vuorinen Vesa, Laurila Tomi, Paulasto-Kröckel Mervi. 2013. Thermodynamic reassessment of Au–Ni–Sn ternary system. Elsevier, Calphad, 43, 61-70. ISSN:0364-5916. DOI:10.1016/j.calphad.2013.10.001

2. Dong Hongqun, Vuorinen Vesa, Tao Xiaoma, Laurila Tomi, Paulasto-Kröckel Mervi. 2014. Thermodynamic reassessment of Au-Cu-Sn ternary system. Elsevier. Journal of Alloys and Compounds, 588 (5), 449-460. ISSN:0925-8388. DOI: 10.1016/j.jallcom.2013.11.041

3. Dong Hongqun, Vuorinen Vesa, Liu Xuwen, Laurila Tomi, Li Jue, Paulasto-Kröckel Mervi. 2016. Microstructural Evolution and Mechanical Properties of Au-20wt.% Sn| Ni Interconnection. Springer. Journal of Electronic Materials, 45(1), 566-575. ISSN: 0361-5235. DOI: 10.1007/s11664-015-4152-3

4. Dong Hongqun, Vuorinen Vesa, Laurila Tomi, Paulasto-Kröckel Mervi. 2016. Microstructural Evolution and Mechanical Properties in (AuSn)eut-Cu interconnections. Springer. Journal of Electronic Materials, 1-9. ISSN: 0361-5235. DOI: 10.1007/s11664-016-4733-9.

5. Dong Hongqun, Vuorinen Vesa, Broas Mikael, Paulasto-Kröckel Mervi. 2016. Thermodynamic Reassessment of the Au-Pt-Sn System and Microstructural evolution of the (AuSn)eut-Pt Interconnection. Journal of Alloys and Compounds, 688, 388-398. ISSN: 0925-8388. DOI: 10.1016/j.jallcom.2016.07.129.

Author's Contribution

Publication I-V:

The research program has been planned together with the co-authors. The author was responsible for writing the manuscripts I-V. In these publications, she conducted all the thermodynamic calculations. The theoretical interpretation of the experimental results were discussed in detail with the co-authors. The microstructural characterization in these five publications were carried out by the author together with Dr. Vesa Vuorinen, with the exception that the STEM/EDX analysis in publication V was conducted by MSc. Mikael Broas. The nanoindentation measurements in Publications III and IV were carried out by Dr. Xuwen Liu.

1. Introduction

Conventional microelectronic packaging is designed to interconnect, power, distribute signals, and cool chips in electronic equipment. The traditional semiconductor packaging is usually classified into [Ohr14]: (i) first-level or device-level packaging: all processes (for example, standard die-/wire- mounting/bonding/encapsulation) involved in packaging individual dies to produce an integrated circuit (IC); (ii) second-level packaging or board level assembly: all the technologies (e.g. surface mount) adopted to assemble two or more of the first-level chip packages onto a printed circuit board (PCB), ceramic substrates, or in assorted multichip modules (MCMs); and (iii) third-level or system-level packaging: interconnection of the boards into a cabinet system. In micro-electro-mechanical system (MEMS) packaging, zero-level packaging has been introduced, for instance, hermetic wafer-level bonding which is necessary for many MEMS devices to encapsulate and protect the active structures.

As the interconnecting material, solder alloys can be applied in all first three levels of packaging [Hwa04, Ohr14]. Normally, the high temperature solder which will not be affected by the subsequent bonding process is required in the zero- and/or first-level of the packaging. Despite the awareness of the threat of lead (Pb) to human life and the environment, high-lead solders (over 85 wt.% Pb) are currently utilized as the die-attach materials for power devices. This is because no proven alternative lead-free alloy for the high-lead solders renders the use of these solders exempted from the RoHS directive (2011/65/EU) [Eil15, EUR]. However, the driving force for lead-free in electrical and electronic devices is not only the technical reasons but the ever-increasing environmental concerns. Consequently, to be lead-free in electrical and electronic equipment, the alternative lead-free solders have to be selected and tested.

Currently, the only possible cost-effective alternatives to lead-free solders are Zn-Al based and Bi-based alloys, however, both of these alloys possess weak bonding strength [Chi11]. The Au-Sn alloy, with a composition of 80wt.%Au and 20wt.%Sn, has been commonly considered as a reliable high temperature solder owing to its excellent mechanical and thermal properties as well as its ability to be bonded without flux [McC06, Sug09, Opp12]. When joining dissimilar materials, the Au-20wt.%Sn alloy (like the majority of solders) cannot directly bond with the covalent materials (i.e. semiconductors and ceramics). In this case, metallization, consisting typically of an adhesion/contact layer and a barrier layer, has to be applied prior to joining. For this purpose different material combinations have been used, such as TiW/Au, Ti/Cu, Ti/Pt, Ti/Mo/Pt,

Ti/Pt/Au or Ni/Au [McN08]. The Ni can be either electroless (2-14 wt.% P) or electrolytic. Regarding the metal substrates, the contact layers are not always required since the metallurgical bond can be achieved due to the reaction between the solder and the substrate. As a consequence, the interfacial reaction at the solder interconnections usually involves at least three elements from the sources of the solder and the contact metallizations (including component metallizations, boards surface finishes and underlying conductors). The reaction between the solder and the conductor metallization system enables the metallurgical bonding by dissolving the solderable metallization into the molten solder and then forming the intermetallic compounds (IMCs) during soldering and solidification. However, if the solderable metallization has been consumed completely, the solder would directly contact the layer (i.e. the substrate or the non-reactive metallization) underneath the metallization. As a result, dewetting of solder could be expected [McN08, Opp05]. In addition, the formation of a thick intermetallic layer at the solder/metallization interface, such as Au-20wt.%Sn solder/Cu heat sink, may degrade the reliability of the solder interconnections due to the brittle nature of the IMCs, the tendency to generate structural defects, as well as the mismatches in physical properties such as the coefficient of thermal expansion (CTE) and elastic modulus [McN08].

On the other hand, the increased miniaturization and ever-growing number of functionalities in microelectronic packages drive the reduction in the size of the joints [Hao15, Lau10a, Koe08]. It was estimated that the diameter of solder joints in flip-chip technology would scale down from 100 μm today to 1 μm in the near future application [Tu13]. Reduction of solder volume eventually lead to different interfacial reactions in smaller solder joints by comparing with those in the larger ones. For instance, the solder joints might be dominated by or even consist only of the intermetallic compounds (IMCs). Therefore, the proper design of the metallization is crucial to obtain robust interconnections.

The traditional way of developing new electronics interconnection materials, including bonding materials and metallization layers, requires long-term experimental investigations and reliability analyses. However, the increasing global competition drives the consumer products today having a time-to-market of only a few months [Lau12]. As a result, it is essential to find an alternative methodology to the time-consuming and costly 'trial and error' approaches. Computer-aided design can significantly reduce the number of development cycles [Li14,]. In order to design a robust interconnection with the maximum level of desired functions, one should understand the relevant phase equilibria in advance, and thus to formulate the microstructure which governs the mechanical and physical properties. Consequently, the CALculation of the PHAse Diagrams (Calphad) approach has been widely accepted as an efficient method of developing a candidate alloy for lead-free soldering by utilizing the theoretical phase diagram modelling [Kro13]. On the other hand, for a given solder/metallization system, the interfacial reaction and the microstructural evolution of the interconnection can be rationalized by combining the experimental results and thermodynamic considerations. Therefore, it is possible to assess the reliability of

the interconnections from the metallurgical viewpoint. In addition to the microstructure of the interconnection, the mechanical properties (e.g. hardness and elastic modulus) of the IMCs significantly influence the reliability of a solder joint. However, since values of the mechanical properties for most IMCs are not well known, further investigation should be conducted on the individual IMCs in order to design reliable metallization systems.

The objective of this dissertation is to design reliable interconnections using Au-20wt.%Sn solder by (i) establishing the entire phase equilibrium of the Au-Sn-X (X=Ni, Cu, Pt) ternary systems; (ii) clarifying the interfacial reactions between the most commonly used contact metallizations and Au-20wt.%Sn solder; (iii) collecting the mechanical properties of the individual intermetallics formed at the solder/conductor interfaces; as well as (iv) identifying the influence of the third elements solubilities on the mechanical properties of the respective interfacial reaction products. The thermodynamic descriptions of Au-Ni-Sn and Au-Cu-Sn ternary systems are presented in Publications I and II in order to establish the global phase equilibrium information for the complex metallization systems. Publications III and IV target (1) rationalizing the equilibrium microstructural evolution of the reaction couple Au-20wt.%Sn| (Ni and Cu) during soldering at 320 °C and subsequently aging at 150 °C based on the authors' experimental results and the basic thermodynamic considerations, (2) collecting the mechanical properties of observed compounds (i.e. AuSn, Au5Sn, (Au,Ni)Sn, (Au,Ni)5Sn (Ni1-x,Aux)3Sn2, (Au,Cu)Sn, (Au,Cu)5Sn and AuCu) by nanoindentation measurements, (3) understanding the influence of the aging (at 150 °C) on the elastic modulus and hardness of AuSn and Au5Sn, (4) identifying the effects of third elements solubilities (i.e. Ni in (Au,Ni)Sn and (Au,Ni)5Sn, Au in (Ni1-x,Aux)3Sn2, and Cu in (Au,Cu)Sn, (Au,Cu)5Sn) on the hardness and indentation modulus of the respective compounds, and thus (5) proposing the potential reliability weakness of the Au-20wt.%Sn|(Ni and Cu) interconnections. In publication V, besides obtaining the thermodynamic descriptions of Au-Pt-Sn, the interfacial reaction that happened at the as-soldered and aged Au-20wt.%Sn|Pt interface were also investigated.

2. Application of Au-20wt.%Sn solder

Au-rich solders, including Au-20wt.%Sn, Au-3wt.%Si, Au-12wt.%Ge and Au-28wt.%In, are all potential candidates for high temperature solder. The Au-20wt.%Sn alloy is the most commonly utilized solder due to a number of reasons. (1) It has a melting temperature of around 280 °C which directly fits the requirement of melting temperature range (270-350 °C) for flip-chip assembly defined by industry in order to ensure efficient process control [Chi11, Zen12]. As shown in the Au-Sn phase diagram (Fig. 1(a)), the Au-20wt.%Sn solder consists of AuSn + hcp at high temperature, while at room temperature it transforms to the Au5Sn + AuSn mixture (Fig. 1 (a)). The equilibrium solidification of Au-20wt.%Sn can be easily followed with the help of the phase fraction diagram (or NP diagram) of Au-20wt.%Sn (Fig. 1 (b)): when temperature decreases to ~280 °C, the liquid transforms to hcp + AuSn immediately; when temperature reaches ~180 °C, the hcp phase will be consumed completely to form Au5Sn due to the reaction hcp + AuSn → Au5Sn, thus to obtain the Au5Sn + AuSn two-phase mixture. (2) Its capability to be reflowed without flux guarantees the application in photonics integration and hermetic encapsulation (especially for vacuum enclosure). (3) Its relatively high creep resistance and yield strength are advantageous for keeping the bond stable during service for a long period. (4) Its high corrosion resistance enables the application in medical devices and some sensors which will operate in corrosive environments. And (5) the high remelting temperature of the Au-rich intermetallics, e.g. 521 °C of hcp-AuSn, promotes Au-20wt.%Sn as a potential transient liquid phase (TLP) bonding material. For instance, the layer structure of Au/Au-20wt.%Sn solder/Au has been applied [Joh05, Opp12, Tol13].

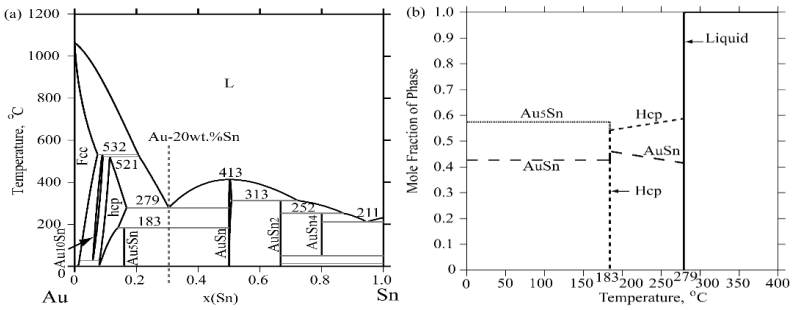

Figure 1. (a) Phase diagram of Au-Sn binary system [Don13]; (b) the NP diagram of Au-20wt.%Sn showing the mole fraction of phases as functions of temperature.

2.1 Die Attach for Power Electronics

Die attach, the first packaging layer in contact with the die, enables the electrical connection between the die and its package. With the miniaturization and increasing demand for the utilization of power devices in high-frequency, high-temperature and high-voltage applications, high-power semiconductor devices must be mounted with a robust die-attach material which fulfill various requirements: (1) high mechanical strength under the normal operating temperature (i.e. ≥ 150 °C); (2) relatively low process temperature thus avoiding adverse effects on the die functionality; (3) high thermomechanical fatigue resistance in order to handle the shear loading stress resulted from the CTE mismatch between the die materials and the mounted substrate; (4) high electrical and thermal conductivities, high chemical corrosion resistance and a high remelting point; and (5) a self-alignment ability to automate the attachment process.

Even though the Pb and Pb-compounds have been known as one of the top 17 chemicals posing the greatest threat to human life and the environment [Abt00], high lead-containing solders, such as Pb-5wt.%Sn and Pb-2wt.%Sn-2.5wt.%Ag, are still utilized as the die attach materials because of the suitable melting temperature range (300 °C–314 °C), excellent mechanical, thermal and electrical properties, wettability, and cost efficiency [Man11], as well as no alternative drop-in solution being available. However, the high lead exemption in RoHS will expire for a large portion of the industry in 2017 unless a technical reason will be provided for extending [Men15]. Therefore, the development of alternative alloys for high-temperature Pb-based solders is of paramount importance. Several alternatives have been proposed, including adhesives, Ag sintering, transient liquid phase sintering, and lead-free solders [Eil15, Men15]. Among these materials, solder is the most preferential type of die bonding material [Ind] because of the robust manufacturing process of soldering [Eil15, Cop07, Man11]. The Au-20wt.%Sn eutectic solder has outperformed most of the lead-free solders as the die attach material for high power applications since it satisfies the requirements, such as relatively high melting point (i.e 280 °C), excellent mechanical properties (strength, and creep resistance), as well as high electrical and thermal conductivities. In addition, it can be utilized with the existing processing equipment. Its potential to be employed in a fluxless process avoids the reliability issues associated with the use of flux. For instance, flux removal of oxides results in undesirable residues [Jia10], and the entrapped residues can cause void formation [Lee05].When the principle of TLP bonding is applied (Au/Au-20wt.%Sn/Au), it allows the creation of an interconnection with a higher remelting point than 280 °C [Rod13] by completely consuming the Au-20wt.%Sn solder to form the Au-rich intermetallics. Even though the Au-20wt.%Sn alloy carries a higher material cost than some other die attach materials, the reliability benefits (summarized in the beginning of this chapter) provided by this alloy often justify this choice, especially, when the TLP die attach process has been adopted [Tol13, Rod13, Kha15, Yin15].

2.2 MEMS Wafer-level Hermetical Encapsulation

The MEMS and IC packaging share some basic functions such as mechanical protection and providing electrical interconnection paths. However, a great variety of the MEMS components contain very fine, freely movable and fragile structures, or otherwise need to operate in a vacuum atmosphere. To optimize performance, those components must be protected in order to keep the fragile component mechanically safe from dust, moisture, or any other kind of physical damage, as well as to form a strictly-controlled operation atmosphere. The cost efficient method of isolating these MEMS components from the external ambient is wafer-level bonding by hermetically-bonding a capping element (i.e. a thin-film layer or a separate wafer) to the device wafer (Fig. 2), since it allows manufacturing and testing of multiple MEMS dies at the wafer-level thus maximizing the throughput, simplifying the process flow and minimizing cost [Tan08, Lau10a].

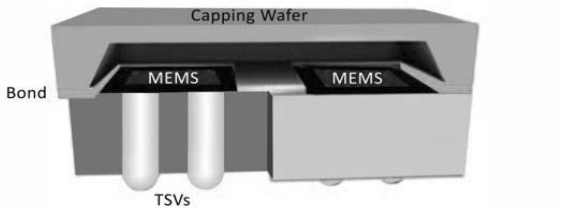

Figure 2. Schematic illustration of capping wafer bonded to MEMS wafer [SPT].

Table 1. Typical wafer-level MEMS bonding methods comparison [Ko09, Esa08, Pau15].

Methods	Advantages	Disadvantages
Glass frit	Simple process; high tolerance for surface roughness; excellent hermetic sealing, good reliability.	High process temperature and cost; Require large seal ring.
Anodic	Proven reliable method in many application; simple process and possible hermetic sealing.	Smooth and clean surface, glass to Si, high DC voltage; residual stress and gas pressure, ion contamination; not CMOS compatible.
Adhesive	Low bonding temperature; comparatively simple, robust and low-cost process; insensitivity to the topography of wafer surfaces.	Not hermetical sealing, outgassing; low tolerance for contamination; pressure-sensitive adhesive provides low bond strengths; unstable properties over time; narrow application temperature range
Metallic	Medium to low bond T, moderate surface roughness requirement, lead-free materials; excellent hermeticity, high joint strength; narrow seal ring geometry; low outgassing, long-term stability; excellent moisture endurance; small footprint.	Intrinsic stress; flow control the molten metal; intrinsic stresses.

Two common methods can be applied to complete the MEMS wafer level packaging, namely thin film packaging (TFP) and wafer bonding (WB). The later one can achieve a higher mechanical strength than the former method, which makes the chip moulding easier. In addition, WB enables creating a suitable vacuum surrounding for the device owning to its larger cavity volume compatibility and more convenient getter integration than TFP [Gar15]. Therefore, WB is a critical part of many MEMS packaging process. The conventionally leading WB methods include glass frit, anodic, adhesive and metallic bonding (Table 1). Metallic

bonding has attracted growing interest for MEMS components encapsulation on wafer-level owing to its outstanding characteristics.

Metal bonding is commonly classified into four classes (Table 2): solder bonding, eutectic bonding, TLP (also known as diffusion soldering, isothermal solidification bonding, or solid liquid interdiffusion bonding) and diffusion bonding [Lin10]. Among them, TLP bonding, combining the planarization capabilities of the eutectic soldering technology with the high remelting temperature of the diffusion bonding process, is the most promising metal bonding method for MEMS packaging [Hoi12, Giu13]. The TLP bonding process involves the following four-step: setting up the bond, heating to the specified bonding temperature to melt the solder and form the liquid in the bond region, holding at the bonding temperature until the last of the liquid interlayer has solidified due to reaction with the parent metals, and homogenizing the bond at a proper heat-treating temperature.

Table 2. Typical metallic wafer bonding [Rei15]

Methods	Advantages	Disadvantages
Solder bonding	Established manufacturing processes; Good self-alignment.	Low re-melting temperature; Bonding strength decrease at elevated temperature; Getter integration difficult.
Eutectic bonding	High re-melting temperature (e.g. 363 °C for Au-Si); High fracture strength joint with Au-Si; CMOS compatible (using Au-Si, and Al-Ge).	Sensitive to chemical surface condition; Long bonding process (1~2 h for Au-Si); Sensitive to heating and cooling rate.
Diffusion bonding	High melting temperature, No risk of metal flow.	High requirement for the surface condition, i.e clean and smooth; high temperature and pressure; long bonding time.
TLP bonding	Hi remelting temperature; High-temperature stability; Moderate processing temperature; Fluxless; Tolerance for surface condition.	Bonding time depending on system; Risk of premature IMCs formation thus to reduce the liquid amount.

The Au-Sn and Cu-Sn metallization systems by far are the most studied alternatives for MEMS wafer bonding [Hoi12, Rei15]. Cu-Sn TLP bonding has the advantage over the Au-Sn TLP bonding in that the price of Cu is cheaper than Au, the IMCs in the Cu-Sn system are thermodynamically more stable than the IMCs of Au-Sn [Rei15]. However, the voids formed in the Cu_3Sn phase could be detrimental to the reliability and stability of Cu-Sn TLP interconnection. Even though methods were proposed to suppress the formation of the voids, such as careful plating process control [Rei15], the reduction of the void amount requires additional efforts [Hoi12]. Compared with the Cu-Sn TLP bonding system, the Au-Sn TLP interconnections have two outstanding features. First, the excellent oxidation resistance of Au promotes the easily implementation of fluxless processes. Second, the remaining Au layer can handle the stress, such as that induced by CTE mismatches when dissimilar materials were interconnected [Hoi12]. For instance, Torleif et al. have demonstrated that the Au-Sn TLP bond joint can absorb the thermo-mechanical stresses induced by the large CTE mismatches between SiC and Cu [Tor13]. Moreover, it has been demonstrated that Au-Sn TLP joints exhibit excellent bonding strength at high temperature, e.g. after aging at 400 °C for 2000 h [Kha15]. All in all, the Au-Sn TLP bonding has appealing properties for MEMS wafer-level encapsulation.

3. Phase Diagram and Thermodynamics

Knowledge of phase equilibria and phase transformations is crucial for nearly all branches of metallurgy and materials science. Phase diagram is the starting point in the optimization of processing variables to formulate a design of the desired microstructure since the chemical and physical properties of a material are basically determined by the microstructure. Even though, in a real system departures from equilibrium will occur, the metastable phase diagrams can be established and the knowledge of the equilibrium state under a given set of conditions (temperature, pressure, chemical composition of the alloy) can offer the insight into the processes (such as solidification, solid-state reaction, phase transformation).

When the Au-20wt.%Sn alloy is employed in the soldering technique, the interfacial reaction involves at least three elements. Even though phase diagrams of many Au-Sn-based ternary systems have been considered complete and final, the repeated investigations, with refinements in apparatus and techniques, lead to their inevitable revision. For instance, the modification of the lattice stability of Sn(hcp) results in the revision of the thermodynamic description of the Au-Sn binary system. As a result, it is essential to modify the thermodynamic descriptions of the relevant higher-order systems. Therefore, the experimental investigations and thermodynamic reassessment of Au-Sn-X (X=Ni, Cu and Pt) are combined in this dissertation in order to establish the reliable equilibrium phase diagrams thus in turn to rationalize the reaction mechanisms of Au-20wt.%Sn solder on contact metallizations (Ni, Cu and Pt).

3.1 Phase Diagram Determination

The methods for phase diagram determination are generally divided into two categories [Zha93, Zha07a]. One category of methods is based on the principle that the properties of a given alloy will vary during the phase transition, such as thermal, physical, chemical and/or mechanical properties. In the second category, the equilibrated alloys and/or diffusion couples or multiples are utilized to study the behavior of a system in an equilibrium or local equilibrium state [Cam12, Zha05]. When the form of phase diagram has been adopted to graphically display the measured phase equilibria, the geometry of all types of equilibrium phase diagrams must obey the Gibbs phase rule [Mas89, Cam12]:

$$f = C - p + 2 \tag{3.1}$$

where f is the number of independent variables (called degrees of freedom), C is the number of components, and p is the number of phases in equilibrium in the system. The number 2 on the right side indicates the two intensive variables, temperature (T) and pressure (P). The construction of phase diagrams cannot violate this rule. The key point of clarifying the state of a system is that one must specify the number of variables involved in.

Even though versatile experimental methods are developed for phase diagram determination, they are generally time consuming and expensive [Zha07a, Zha07b, Cam12]. For instance, extremely long annealing time will be required in order to acquire the phase equilibrium at low temperature, since the diffusivity of atoms is generally low at temperatures below half of the melting point [Oht08]. The complexity of real materials results in increasing difficulties in phase diagram determination. In some cases, even a minor contamination can result in a significant difference in the phase equilibria [Smi07]. Moreover, it is rather difficult to establish the multicomponent phase diagrams over wide ranges of compositions and temperatures by only applying experimental investigations.

Nevertheless, a phase diagram is a representation of the thermodynamic relationships between competing phases. Theoretically, phase diagram can be constructed when reliable models are available for the description of Gibbs energies of all phases in dependence on temperature and composition. Therefore, the computational methods have emerged and established their place in design and study of complex and modern alloys. The Calphad approach enables us to rapidly obtain multicomponent phase diagrams based on sufficient amount of reliable experimentally determined data for lower-order systems and their combination with physically sound models for Gibbs energy description [Oht98].

3.2 Thermodynamic Calculation

Calphad approach was initiated by Larry Kaufman et al. in 1970 [Kau70]. As one of the computational methods, it is employed to model the underlying thermochemical properties of each phase. The general principle of the Calphad approach is based on the well-known second law of thermodynamics that a system with a given set of conditions (temperature, composition and pressure) reaches the state of lowest Gibbs energy. If the Gibbs energy (as a function of temperature, composition and pressure) is obtained for individual phases, it is possible to calculate the equilibrium states according to the energy minimization procedure. On the other hand, the experimental measurements (i.e. for thermodynamic properties of individual phases and the phase equilibria) are essential, since the validated databases are based on the combination of the reliable and sufficient set of theoretical and experimental data (Fig. 3).

According to Schmid-Fetzer and Gröbner [Sch01], the Calphad approach has several distinct advantages:

This method enables researchers to extrapolate the thermodynamic descriptions and phase equilibrium calculation from the assessed binary systems to ternary and higher order systems, which is the essential feature for the application to industrial situations.

It can help to drastically reduce the necessary experimental efforts in multicomponent systems by identifying the relevant key experiments.

Both stable and metastable phase equilibria can be calculated by simply suspending the individual phases which do not form under specific conditions.

The driving forces for all phase transformations can be calculated, which is crucial for simulation of microstructural evolution. The local phase equilibria can also be calculated thus providing the numerical input to materials processing simulation, such as the solidification simulation.

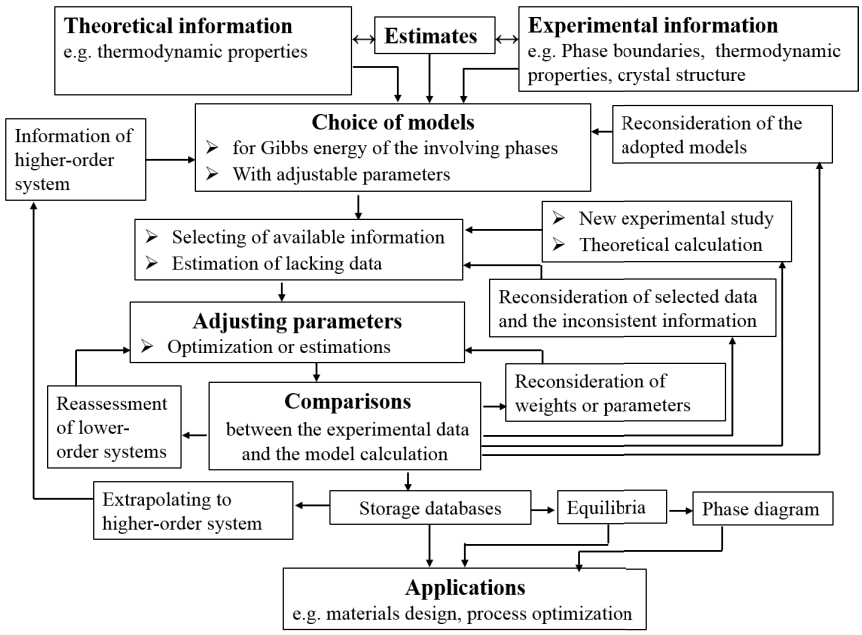

Figure 3. Sketch of the Calphad approach, combining thermodynamic modelling with key experiments.

3.2.1 Thermodynamic Criterion for Equilibrium

Gibbs energy (G) is the most commonly used functions for specifying the equilibrium conditions of a system: *in an isothermal, isobaric system with constant amounts of all components, the equilibrium is reached when the Gibbs energy reached its minimal values* [Luko7a]. It is expressed as

$$G = U + P \cdot V - T \cdot S \tag{3.2}$$

where U, V and S denote the internal energy, volume and entropy of the system. The change in Gibbs energy of a closed system undergoing a process is

$$dG = dU + P \cdot dV + V \cdot dP - T \cdot dS - S \cdot dT \tag{3.3}$$

Where
$$dU = T \cdot dS - P \cdot dV \tag{3.4}$$

Therefore
$$dG = V \cdot dP - S \cdot dT \tag{3.5}$$

The change in G is defined by the two independent variables: absolute temperature and pressure. For a closed system, when the pressure and temperature are constant, the change in G of the system at equilibrium with its surroundings is zero.

In a multicomponent system, the variable composition (N_i: the number of moles of components i) is introduced in the Gibbs energy function

$$G = f(P, T, N_i) \tag{3.6}$$

Regarding a single phase in a binary system of A-B undergoing a reversible process, the change in G of this phase is now given as

$$dG = \frac{\partial G}{\partial P} \cdot dP + \frac{\partial G}{\partial T} \cdot dT + \frac{\partial G}{\partial N_A} \cdot dN_A + \frac{\partial G}{\partial N_B} \cdot dN_B \tag{3.7}$$

Here, N_A and N_B are the number of moles of A and B. The quantity $\frac{\partial G}{\partial N_i}$ is the chemical potential of component i and is denoted as μ_i. The chemical potential μ_i is identical to the partial molar Gibbs energy $\overline{G_i}$ ($\overline{G_i} = (\frac{\partial G}{\partial N_i})_{T,P,N_j}$, $i \neq j$) for component i. In equilibrium, the partial molar Gibbs energy $\overline{G_i}$ of all components i in each pair of different phases are equal (such as $\overline{G_A^\alpha}(T,P,N_A^\alpha) = \overline{G_A^\beta}(T,P,N_A^\beta)$ and $\overline{G_B^\alpha}(T,P,N_B^\alpha) = \overline{G_B^\beta}(T,P,N_B^\beta)$) [Luko7a]. Therefore, it is evident that the chemical potential of a component is uniform in each pair of different phases ($\alpha, \beta, \gamma, \ldots, \omega$) of an equilibrium system, i.e.

$$\mu_i^\alpha = \mu_i^\beta = \mu_i^\gamma = \ldots = \mu_i^\varpi \tag{3.8}$$

Even though, the equal chemical potential criterion is very useful, it still has limitation: when the composition of component i in a solution is close to the value of zero ($x_i \to 0$), the chemical potential of i then tends to negative infinity ($\mu_i \to -\infty$). Nevertheless, this shortcoming can be overcome by introducing the activity of the component

$$\mu_i = {}^0\mu_i + R \cdot T \cdot ln(a_i) \tag{3.9}$$

Where ${}^0\mu_i$ is the chemical potential of pure component i in a given standard state, it can be replaced by the molar free energy of pure i (${}^0G_i$). However, if ${}^0G_i$ is adopted, the reference state of the pure element has to be clarified. Letter R is the gas constant and a_i the activity of component i in the solution. Therefore, according to equation (3.8) it is evident that, component i also has identical activity in each pair of different phases present in an equilibrium system, i.e.

$$a_i^\alpha = a_i^\beta = a_i^\gamma = \ldots = a_i^\varpi \tag{3.10}$$

3.2.2 Modelling of Gibbs Energy

The complete description of a thermodynamic system requires the specification of the temperature, pressure and compositions of existing phases [Bak92]. The aim of the modeling is to find a state with minimum total Gibbs energy for a given set of independent conditions (i.e. pressure, temperature, overall concentration). The total Gibbs energy G can be expressed as the weighted sum of Gibbs energies of all phases that take part in the equilibrium. In the Calphad

approach, a variety of models are employed to describe the Gibbs energy of individual phases. The contributions to the Gibbs energy of a phase ϕ can be written as

$$G_m^\phi = G_{ref}^\phi + T \cdot {}^{cnf}S^\phi + G_{ex}^\phi + G_{mag}^\phi + G_p^\phi + G_{surf}^\phi + \ldots \tag{3.11}$$

The term G_{ref}^ϕ (reference) is the weighted sum of the molar Gibbs energies of all the constituents (i.e. elements or compounds) in the crystallographic structure corresponding to the structure of the given phase, relative to the selected reference states. Normally, the pure solid elements in their stable states at 298.15 K and normal pressure are taken as the reference states (so-called standard element reference (SER) state). In 1991, Dinsdale has published the Gibbs energies as a function of temperature (from 298.15 K, or in some cases 200 K) for stable and metastable states of pure elements [Din91]. The latest version of the unary database can be freely downloaded online (Scientific Group Thermodata Europe - SGTE) [SGTE]. For the substitutional solution phase (both solid and liquid), G_{ref}^ϕ can be generally expressed by the mechanical mixing of respective reference states of constituents

$$G_{ref}^\phi = \sum_{i=1}^{n} x_i \cdot {}^0G_i^\phi \tag{3.12}$$

where x_i is the molar fraction of components. The temperature dependence of the term of ${}^0G_i^\phi$ is usually expressed as a power series of temperature

$${}^0G_i^\phi = c_1 + c_2 \cdot T + c_3 \cdot T \cdot ln(T) + \sum c_n \cdot T^z \tag{3.13}$$

where $c_1, c_2, \ldots, c_n$ are coefficients. Letter 'z' is the integers.

The second term, ${}^{cnf}S^\phi$ stands for the configurational entropy of the phase. For an ideal random mixing of the constituents ($i=1, 2, 3 \ldots n$) on the crystal lattice, its contribution to the total Gibbs energy is described in this form

$$S_{id}^\phi = R \cdot \sum_{i}^{n} (x_i \cdot ln(x_i)) \tag{3.14}$$

The third term, G_{ex}^ϕ, is the excess Gibbs energy. It describes the real behavior of the phase and includes all contributions not covered by Eq. 3.11, such as vibrational and electronic contributions. The mostly utilized excess model is the Muggianu's extension of the Redlich-Kister series since it is symmetrical and thus extrapolates well to ternary and even higher-order systems [Kro12, Luk07b]

$$G_{ex}^\phi = \sum_{i=1}^{n-1} \sum_{j=i+1}^{n} x_i x_j L_{ij} + \sum_{i=1}^{n-2} \sum_{j=i+1}^{n-1} \sum_{k=j+1}^{n} x_i x_j x_k L_{ijk} + \ldots \tag{3.15}$$

The interaction parameters are

$$L_{ij} = \sum_{v=0}^{y} (x_i - x_j)^v \cdot L_{ij}^v \tag{3.16}$$

$$L_{ijk} = v_i \cdot L_{ijk}^i + v_j \cdot L_{ijk}^j + v_k \cdot L_{ijk}^k \tag{3.17}$$

$$\begin{aligned} v_i &= x_i + (1 - x_i - x_j - x_k)/3 \\ v_j &= x_j + (1 - x_i - x_j - x_k)/3 \\ v_k &= x_k + (1 - x_i - x_j - x_k)/3 \end{aligned} \tag{3.18}$$

The introduced v_i fractions render the symmetrical behaviors of the ternary parameters in higher-order systems [Hil80]. The compositional independent ternary parameter will be obtained, if all L_{ijk}^{i} were identical.

The last three terms of Eq. 3.11 are: (i) the magnetic contribution G_{mag}^{ϕ} which is significant if the material exhibits magnetic behavior; (ii) the contribution from pressure-dependent properties G_{P}^{ϕ}; and (iii) the contribution of surface energy G_{surf}^{ϕ} which requires great attention in the case of nanomaterials.

3.2.3 Driving Force for Interfacial Reaction

From the thermodynamic viewpoint, for a closed system at a given set of conditions (constant pressure and temperature) the chemical reaction occurs towards the direction which can minimize the total Gibbs free energy of the system. In other words, the driving force of the chemical reaction is the differences of the change in the Gibbs energy of the reaction. A chemical reaction can be presented as

$$r_1R_1 + r_2R_2 + \ldots = p_1P_1 + p_2P_2 + \ldots \tag{3.19}$$

where r_1, r_2,... are the number of moles of the reactants R_1, R_2,... and p_1, p_2,... are the number of moles of the products P_1, P_2,....And the change in the Gibbs energy can be described as [Gok75]

$$\Delta G = \sum p_i \overline{G_{p_i}} - \sum r_i \overline{G_{R_i}} \tag{3.20}$$

here $\overline{G}_{P_i}$ and $\overline{G}_{R_i}$ are the partial molar Gibbs energy of products (P_i) and reactants (R_i).

If the change in the Gibbs energy of the reaction is negative, the chemical reaction of Eq. (3.19) is thermodynamically allowed and will proceed spontaneously at constant temperature and pressure in the forward direction (reactants to products) unless the kinetic barriers are present. On the other hand, if $\Delta G > 0$ the reaction spontaneously proceeds in the backward direction (products to reactants).

Since the chemical reaction occurs at a constant pressure and temperature, the changes in the thermodynamic properties are only those accompanying the reaction. When substituting the partial mole Gibbs free energy of the condensed products and reactants ($\overline{G_i} = G_i^o + R \cdot T \cdot ln(a_i)$), Eq. (3.20) can be rewritten as

$$\Delta G = \sum p_i G_{P_i}^0 - \sum r_i G_{R_i}^0 + R \cdot T \cdot \sum p_i \, ln(a_{P_i}) - R \cdot T \cdot \sum r_i \, ln(a_{R_i}) \tag{3.21}$$

By giving the change in the standard Gibbs free energy of the reaction ($\Delta_r G^0 = \sum p_i G_{P_i}^o - \sum r_i G_{R_i}^o$) and separating the logarithmic terms from others, Eq. (3.22) will transform into

$$\Delta G = \Delta_r G^0 + R * T * ln\left(\frac{a_{P_1}^{p_1} \cdot a_{P_2}^{p_2} \cdot \ldots}{a_{R_1}^{r_1} \cdot a_{R_2}^{r_2} \cdot \ldots}\right) \tag{3.22}$$

At equilibrium, ΔG is zero. The activity ratio in the parentheses is a constant when temperature and pressure are constant. Eq. (3.22) can also be applied in non-equilibrium conditions, in which the activities in the phases are based on the randomly chosen concentrations [Lau10b].

4. Microstructural and Mechanical Characterization

The well-known material science tetrahedron (Fig. 4(a)) indicates the strong interactions among the four major components of material science and engineering, i.e. the processing, structure, properties and performance of materials. The systems materials engineering triangle (Fig. 4(b)) also reveals that the comprehensive knowledge on the individual materials components is the critical starting point for system-level planning of research.

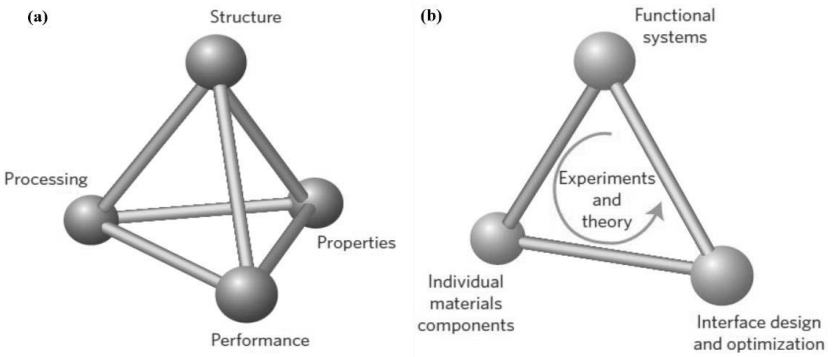

Figure 4. The traditional material science tetrahedron (a) and the engineering systems materials engineering triangle (b) [Yan12].

4.1 Microstructural Characterization

Characterization of microstructure involves revealing the fundamental features from three aspects: (i) to identify the different crystallographic phases which are presented in the sample, (ii) to characterize the morphology of these phases, and (iii) to determine the local elemental composition [Zin09]. In general, the structural and chemical characterizations are realized based on the interaction between an equipped probe (such as the visible light, X-rays, high energy electron beam) and a carefully prepared specimen (Fig. 5). Once the probe has interacted with the sample (sample surface or bulk), the scattered or excited signals are generated and then collected and stored in an image plane. The selected data is then read out and processed into a form which can be interpreted. For instance, in microscopy, the signal can be presented as a two-dimensional

image of the sample; in microanalysis, one can obtain a spectrum in which the signal intensity is recorded as a function of its energy or wavelength; and in diffraction, the signal is shown in the form of either a diffraction pattern or a diffraction spectrum.

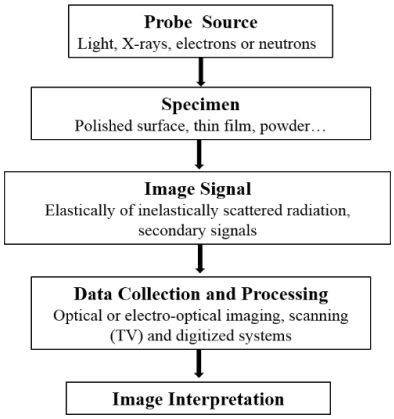

Figure 5. Schematic illustration of the microstructural characterization relying on the interaction of materials with a probe [Bra08].

Currently, a variety of state-of-the-art technologies are available for microstructural characterization. To identify the structural feature of a sample, one can employ scanning electron microscopy (SEM), transmission electron microscopy (TEM), scanning transmission electron microscopy (STEM), focused iron beam (FIB), scanning acoustic microscopy (SAM), X-ray diffraction among numerous others [[Exn96, Exn04].]. In regard to chemical composition analysis, various commercial instruments are available, including auger electron spectroscopy (AES), electron probe micro-analyzer (EPMA), energy-dispersive X-ray spectroscopy equipped either in SEM (SEM-EDX) or TEM (TEM-EDX), Rutherford backscattering spectrometry (RBS) and others [Ber15, Has08, Jey11, Kar95, Kub15, Män16, Mor14, and Wil92,]. A short summary of basic information for some techniques are listed in Tables 3 and 4.

Table 3. Basic properties of some techniques applied for structural characterization [after Exn96, Exn04 and Män16]

	SEM	TEM	STEM	FIB	SAM
Probe	Electron	Electron	Electron	Ion	Acoustical waves
Detected signal	Electron	Electron	Electron	Electron/Ion	Acoustical waves
Depth resolution	~ 1µm	5 nm	5 nm	1 nm	<100 nm
Lateral resolution	2nm	0.1 nm	0.2 nm	10 nm	20-50 µm
Penetration depth	1-5 µm	500 nm	500 nm	20-50 nm	50-100 µm
Information	Surface topography, compositional contrast, crystal orientation	Crystallographic, morphologic, topographical and compositional information	Topographical information, Z^1- contrast,	Topographical and morphologic information, Chemical differences	tomography
[1] Z represents the atomic number of elements					

Table 4. Basic properties of some techniques applied for chemical characterization [Män16, Ber15, Bru10, Jey11 and Wil92]

	AES	EPMA	SEM-EDX	STEM-EDX	RBS
Probe	Electrons	Electrons	Electrons	Electrons	He ions
Detected signal	Electrons	X-rays	X-rays	X-rays	He ions
Depth resolution	1-10 nm	0.1-2 µm	50-1000 nm	Sample thickness	> 2 nm
Lateral Resolution		170 nm	1 µm	< 50 nm	> 500 µm
Elements detected	From Li	From Be	From Be	From Be	From B
Detection limit	< 1 at.%	~ 10 ppm	< 1 at.%	< 1 at.%	< 1 at.%
Chemical-state information	Limited	Limited	No	no	limited
Depth profiling	Down to 1 µm	Yes, but limited	no	no	Down to 20 µm

In the thesis, the diffusion couple method has been adopted to study the Au-20wt.%Sn|X (X=Ni, Cu, Pt) samples. In this technique, phase boundaries are located by taking advantage of the local equilibrium at the phase interfaces in the diffusion zone. For instance, a diffusion couple made up of two different materials is isothermally annealed at a desired temperature over a sufficiently long period in order to achieve the stable equilibrium state over the specimens. Consequently, the sandwich-like bulk samples were prepared by placing 100 µm of Au-20wt.%Sn between 100 µm of Ni, Cu and Pt foils. Provided that the total thickness of samples utilized in the dissertation work are around 300 µm, the resolution of SEM and SEM/EDX analysis is capable to identify most of the phases. Besides, extensively experimental works have already been published to present the reactions that have been observed at Au-20wt.%Sn|X interfaces, these previous experimental results can help the interpretation of the present studies. On the other hand, phase diagrams of Au-Sn-X (Ni, Cu and Pt) were established with the method of Calphad approach. Thermodynamic equilibria can assist the identification of the equilibrium reaction products in respective interconnections. Thus, SEM with EDX were mainly employed to study the microstructural characterizations of Au-20wt.%Sn|X (X=Ni, Cu, Pt) interconnections. A piece of equipment with higher resolution than SEM/EDX was required to reveal the delicate details of the interfacial microstructure of aged Au-20wt.%Sn|Pt samples. Therefore STEM with EDX was adopted.

4.2 Nanoindentation

Nanoindentation, has also been known as instrumented indentation or depth-sensing indentation [Bul75, Poo08 and Ter74]. It is capable to evaluate different kinds of mechanical properties (hardness, elastic modulus, hardening exponents, creep parameters and residual stresses) and to identify nanoscale phenomena (defect nucleation and dynamics, strain localization, and phase transformation) [Oli04, Sch06]. Most commonly, nanoindentation tests have been utilized to measure the hardness and the elastic modulus of materials by using load and depth sensing indentation techniques [Ant11, Cho10, Sch06 and Oli92].

In this work, the hardness and indentation modulus of the major interfacial reaction products of Au-20wt.%Sn|X (X= Cu and Ni) were measured using a

TriboIndenter® (Hysitron Inc., USA) nanomechanical testing instrument. A diamond cube-corner indenter (normal tip radius around 40 nm) has been adopted which served both for the indentation tests and as the scanning probe microscopy (SPM) tip during imaging. The locations of the tip with respect to the desired phases were determined on the basis of the images obtained via the pre-scanning of the specimen. All measurements were performed under a load-control model. The indentation test consisted of three steps: a loading segment, a rates of 10 or 25 μN/s, to a maximum load of 100 or 250 μN, followed by a hold segment for 5 s, and finally, unloading at rates of 20 or 50 μN/s. After each indentation, the SPM imaging was carried out to determine the locations of the indents. The nanoindentation system was calibrated prior to testing by performing indentation tests on a fused quartz standard. The compliance of the load frame and the area function for the indenter were measured and periodically checked. Measurements of reduced modulus and hardness were performed via the Oliver and Pharr method [Oli92, Oli94].

5. Results

Nickel, copper and platinum are the three most commonly encountered contact metallizations for Au-20wt.%Sn solder. The interfacial reaction of Au-20wt.%Sn solder on the conductor X (X=Ni, Cu, Pt) is expected to vary with different soldering processes and the thermal histories of the bonded joints. Phase transformation in solder joints can be diverse with the following stages. At melting stage, atoms from the contact metallization will dissolve and react with the species in molten solder. During solidification, several processes will be included, such as nucleation, precipitation on preexisting phases, and metastable phase formation. In subsequent integration processes and during usages, the phenomena are interdiffusion, coarsening, reaction with the contactor in the solid state, as well as changes in the solubilities and the distribution of phases resulting from thermomechanical fatigue. It is widely accepted that the well-established thermodynamic descriptions benefit not only the rationalization of the interfacial reactions but also the thermodynamic prediction of the potential interfacial products by calculating phase diagrams and thermodynamic properties. On the other hand, the brittle nature of the interfacial products is widely accepted as the detrimental effect on the reliability of an electronic interconnection. Therefore, it is of great interest to understand the microstructural evolution of the solder joints at liquid and solid stages, as well as the individual hardness and elastic modulus of the IMCs formed at the interface.

5.1 Microstructure

5.1.1 Au-20wt.%Sn|Ni System

Phase diagram of the Au-Ni-Sn ternary system has been established experimentally [Neu96, Liu05] and thermodynamically [Liu05]. However, the thermodynamic description of the Au-Sn binary system in literature [Liu05] did not use the modified lattice stability of the unary Sn(hcp) [SGTE] and the updated thermodynamic description of Ni-Sn [Zem12]. In order to be compatible with Au-Sn-based higher-order multicomponent systems, the Au-Ni-Sn ternary system has been reassessed in this work (Publication I) based on the present experimental investigation of Au-20wt.%Sn|Ni reaction couples, the reported phase equilibria [Liu05, Neu96, Sch07], and the thermodynamic information [Dęb10, SGTE]. The thermodynamic descriptions of all three binary subsystems

have been take from the literature: Au-Ni is according to [Wan05], Au-Sn is according to [Don13], and Ni-Sn is according to [Zem12] except for the parameters of Ni3Sn4. The parameters of Ni3Sn4 phase was modified on the basis of the model described in [Zem12], in order to fit the reported homogeneity ranges [Sch07].

Solid/liquid interfacial reaction

Microstructural characterization of Au-Sn/Ni has been extensively investigated, as briefly summarized in Table 5. The interfacial reaction involved in molten solder and Ni contact metallization has been investigated at the temperature range of 290-350 °C. The intermetallics formed at the Au-20wt.%Sn/Ni interface are either AuSn(Ni) [Yoo09], AuSn(Ni)+Ni3Sn2(Au) [Son01], or Ni3Sn2(Au) [Yoo07a, Yoo09, Wei13, Xu14 and Rau15], hereafter, the certain element listed in the parentheses represent that the respective phase dissolves that given third element. The different experimental configurations in the literature render difficulty in comparing the results from various publications directly. Nevertheless, the general trend can be extrapolated: AuSn(Ni) displayed at the solder/Ni interface when Au-Sn|Ni reaction couples were bonded at low temperature or reflowed for a short time [Tas05, Tsa06, Yoo09]; once the samples were subjected to a high bonding temperature or a long soldering period, the Ni3Sn2(Au) layer was formed on top of Ni [Yoo07a, Yoo09, Xu14, Rau15]. The result in [Wei13] represents an exception to the proposed conclusion that when samples were reflowed at 300 °C for only 90 s the Ni3Sn2(Au) layer has already been formed at the solder/Ni interface. Nevertheless, such exception is understandable since Ni dissolves faster in the liquid via finer grains of Ni resulted from the electroplating. However, these previous publications focused on presenting the observed phenomena rather than rationalizing the reaction mechanism.

In the present experimental study, it was noticed that AuSn(Ni) phase dominated the solder/Ni interface after bonded at 320 °C for 100 seconds (Fig. 6(a)), while this intermetallics was replaced by Ni3Sn2(Au) after 10000 s of soldering at 320 °C (Fig. 6(b)). This reaction phenomenon is consistent with the results in [Son09]. The microstructure observed in this work (Fig. 6(a)) was understandable on the basis of the calculated isothermal and vertical sections (Fig. 7) (in Publication III).

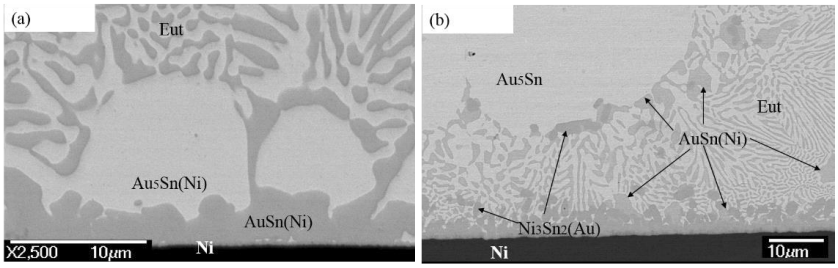

Figure 6. SEM-BSE images of the Au-20wt.%Sn|Ni joints soldered at 320 °C for: (a) 100s and (b) 10000 s.

Table 5. Summary of Au-Sn|Ni interfacial reactions investigations

Ref.	Sample	Thermal condition	Method	Statements
[Lee92] [Kat94]	E-beam evap. 0.2Ti/0.3Ni/3.2(Au/ Sn stack, 64.4 at.% Au)	320 °C, 1, 3, 5 min,	AES-depth profile	Prior to reflow: Au, Sn have intermixed completely with each other. During reflow, Ni dissolved into solder, Au and Sn dissolved into Ni as well while the penetration of Au into Ni was less than that of Sn; ternary intermetallics (containing Ni, Sn, Au) were formed. After 1 min, only 100 out of 300 nm Ni was left. After 3 min of reflow, only the 50 nm Ni (mixed with Ti) was left. After 5 min, Sn penetrated to Ni/Ti.
[Son01]	Z-MAJICTM bump (dia:150-160^{Uint}, tall: 45-50) Eut/0.1Au/5 electroless Ni/12Cu	Reflow: 280-315 °C, 75 s	SEM-EDX TEM-EDX	Bulk of solder: predominated with large islands of Au_5Sn. At the interface: almost layered coarse AuSn(5-8Ni*) phase and irregular-shaped Ni_3Sn_2(22-25Au) phase. TEM/EDX results of the as-solidified bump: Ni_3Sn_2(Au)/0.16-0.18 µm amorphous layer with composition of 7-10Au60-65Ni13-20Sn9-13P/0.15-0.2 µm fine-grained P-rich (22-23 at.%P) region/a fine-grained Ni-P (5-8 at.%P) layer/Cu substrate.
		Aging: 200 °C, up to 365 d		Bulk solder: coarsening with aging. At the interface: AuSn adjacent to the interfacial layer was replaced by Au_5Sn then to form Ni_3Sn_2(22-26Au)/AuSn(21-24Ni)/Au_5Sn(<1Ni). Interface of Ni_3Sn_2(Au) became flat and thickness of total interfacial intermetallic layers grew with the square root of aging time at 200 °C.
[Par02]	Evap. Eut/RF sputtering Ni	330 °C, 0-7 min	SEM-EDX	Thickness of interfacial reaction product grew with time. It was ~6.5 µm after 300 s of reflow.
[Tsa05] [Tsa06]	Evap. 2.5Sn/3.75Au/2Ni	290 °C, 2min	SEM, EPMA XRD	Above Ni: AuSn(8.6Ni)layer/ mixture of AuSn(Ni), Au_5Sn(1.1Ni).
		240 °C, 2 min		Layer: Ni/Au_5Sn(1.5Ni)/AuSn(1Ni).
		290 °C, 2 min, 240 °C, 4, 72 h		Consisting of: Au_5Sn(3Ni)/AuSn(14.5Ni)+Au_5Sn(Ni) coarse mixture/AuSn(Ni)/ Ni_3Sn_2(20-22Au)/Ni. The Ni_3Sn_2(Au) (i.e. 20-22Au34-35Ni43-44Sn) layer formed after aging for 72 hours.
		240 °C, 2 min, 240 °C, to 1000 h		Another AuSn(Ni) layer formed above Ni. 1 hours: AuSn(Ni)/Au_5Sn(Ni) /AuSn(Ni)/Ni to, 4 hours: AuSn(1Ni)+Au_5Sn(Ni)/Au_5Sn(3Ni)/AuSn(11Ni)/Ni to, 9 and 72 hours: Au_5Sn(0.9Ni)/AuSn(20Ni)/ Ni_3Sn_2(Au)/Ni. Thickness of AuSn(Ni) and Ni_3Sn_2(Au) grew with time. 208 hours: Au_5Sn(Ni)/AuSn(Ni)/ Ni_3Sn_2(Au)/Ni to, 1000 hours: Au_5Sn(0.9Ni)/ Ni_3Sn_2(23Au)/a ternary compound Au-Ni-Sn/Ni.
[Yoo07a]	0.2Ti/0.8Cu/10 Ni(electroplate)/35Eut(coelectroplated)	Max. temperature 320 °C for 60 s	SEM-EDX EPMA	Bulk solder: fine eutectic microstructure and the coarse Au_5Sn+AuSn two-phase areas. At the interface: one reaction product Ni_3Sn_2(Au) with composition of 29.8Au30.1Ni40.1Sn.
		Aging: 150 °C, 100, 500, 1000 h		AuSn(Ni) layer with a composition of 32.4Au19.7Ni47.9Sn. The thickness of AuSn(Ni) layer slightly increased with aging time.
		Aging: 250 °C, 100, 500, 1000 h		This interfacial reaction product AuSn(Ni) consisted of Ni-rich AuSn(28, 31.8, 28.9 and 28.7Ni) and Au-rich AuSn(13.6, 18, 19.8 and 19.6Ni) with contrast difference. After 1000 hours of aging, a new IMC layer Ni_3Sn_2(18.4Au), and a crack formed at AuSn(Ni)/ Ni_3Sn_2(Au) interface. Interfacial layers: Au_5Sn/AuSn(Ni)/ Ni_3Sn_2(Au).

[Yoo09]	Cu/5Ni(15at.%P)/0.15Au/Eut (foil)	Max. temperature 310 °C for 60 s	SEM-EDX EPMA	As-bonded: forming layered AuSn(Ni) with composition of 34.8Au17.4Ni47.8Sn /Ni3P/Ni(P)/Cu.
		Reflow: 310 °C, 5, 15, 30 min		Bulk solder: long and large AuSn(Ni) near interface; At solder/Ni(15P) interface: Ni_3Sn_2(Au) (i.e. 27.2Au33.7Ni39.1Sn)/Ni_3P with Kirkendall voids formed inside; Ni_3Sn_2(Au) grew into solder and attached to AuSn(Ni); After 15 min, Solder penetrated into Ni(P) layer.
		150 °C, to 1000 h		As-aged: at interface: only AuSn(Ni). Bulk solder: coursing with increasing aging time.
		Aging: 250 °C, to 1000 h		Solder bulk: coarse AuSn+Au_5Sn. At the interface: 100 hours: AuSn/AuSn(17.7Ni); 250 to 500 hours: AuSn layer above AuSn(Ni) was gradually transformed into Au_5Sn, AuSn(17.7, 12Ni) became thick, and inside Ni_3P layer formed columnar-like voids. Au and Sn penetrated into Ni_3P. 1000 hours: AuSn(Ni) divided into Au-rich AuSn(10Ni) and Ni-rich AuSn(24.7Ni) two layers with contrast difference. Ni(P) transformed into P-rich Ni_5P_4 (57.34Ni41.39P1.23Cu0.04Sn). Solder reacted with Cu substrate to form AuCu and $AuCu_3$. Interfacial layers:Au_5Sn/AuSn(Ni) Au-rich/AuSn(Ni) Ni-rich/AuCu/$AuCu_3$.
[Wei13]	Cu/15Ni-electro-plated/50Eut(cold rolled 3x Au/Sn layers, then aged at 220 °C,14 h)	Bonding: 300 °C, 90 s	SEM-EDX	Bulk solder: fine eutectic microstructure and coarse Au_5Sn(Ni), AuSn(Ni) and Ni_3Sn_2(Au).At the interface: a thin Ni_3Sn_2(Au) layer.
		Aging: 150 °C, to 1000 h		Bulk solder: coarsening significantly with aging for 100, 300, 500 and 1000 h. At the interface: irregular AuSn(Ni)/ Ni_3Sn_2(Au) layers.
		Aging: 200 °C, to 1000 h		Bulk solder: Up to 300 h, Ni_3Sn_2(Au) was formed inside AuSn(Ni); Structure transformed from AuSn(Ni)+Au_5Sn(Ni) to Au_5Sn(Ni) layer after 500 h. At interface: Au_5Sn(Ni) /AuSn(Ni) layer which slightly thickened till 300 h/Ni_3Sn_2(Au) became flat from 500 h of aging.
[Xu14] [Rau15]	0.04TiW/0.2Ti/ electroplated (6Au/2Sn)	350 °C, 60 min	SEM-EDX	Layed: Au_5Sn/ Ni_3Sn_2(Au) with composition of 25Au35Ni40Sn.
This work	Foils: 100Ni/100Eut/100 Ni	Bonding: 320 °C, 100 s	SEM-EDX	Bulk solder: composed of fine eutectic microstructure in the middle, as well as large Au_5Sn(2.1Ni) islands and irregular layered AuSn(4.7Ni) near the interface.
		Aging: 320 °C, 2500, 10000 s		Bulk solder: near the interface, Au_5Sn(Ni) and AuSn(Ni) depleted up to 10000 s of annealing. At the interface: Ni_3Sn_2(33Au) layer with irregular interface at the solder matrix side was formed and grew with increasing annealing time.
		Aging: 150 °C, to 4600 h		Bulk solder: dominated by eutectic structure with coarse AuSn(3Ni) and Au_5Sn(3.5Ni) growing towards the middle of the solder matrix. At the interface: Ni_3Sn_2(32Au)/Ni_3Sn regular layers were formed on top of Ni. Thicknesses of these layers grew with increasing annealing time. AuSn(Ni) phase formed on top of Ni_3Sn_2(Au) was replaced by Au_5Sn(Ni).
Uint The units for all layers are µm; * data shown in parentheses indicates the mole fraction of the dissolved third element; Eut means Au-20wt.%Sn solder.				

It can be anticipated from the phase equilibria (Fig. 7(a)) that the Ni3Sn2(Au) layer will became the main interfacial reaction product at the sol-der/Ni interface in the prolonged bonding duration. When the samples were bonded for a longer period (e.g. to 10000 s of soldering in the present study), Ni atoms from Ni layer will continuously diffuse into the pre-existing intermetallic layer of AuSn(Ni). The formation of Ni3Sn2(Au) can be ascribed to the signifi-cantly high solubilities of Ni in AuSn(Ni) (i.e. ~ 11 at.% Ni) and Au in Ni3Sn2(Au) (up to 33 at.% Au) which are promoted by the similar lattice struc-ture of AuSn (NiAs) and Ni3Sn2 (Ni2In), as well as the same crystal structure and similar lattice parameters of Au (fcc, a=0.4072 nm [Vil97a]) and Ni (fcc, a=0.35236 nm [Vil97b]). When Ni content in AuSn exceeds the solubility of Ni in this compound, the reaction of Ni with AuSn(Ni) results in the formation of Ni3Sn2(Au) at the bond extremity probably by replacing the Au with Ni in AuSn(Ni).

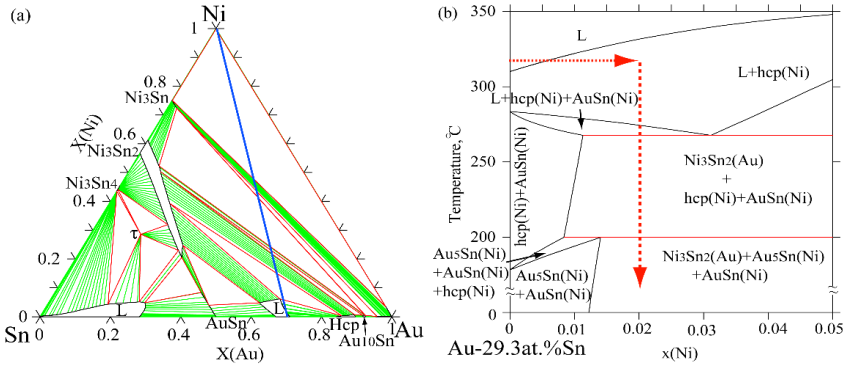

Figure 7. Calculated phase equilibrium (a) isothermal section of Au-Ni-Sn at 320 °C, and (b) vertical section of (AuSn)eut-67.2Au27.8Sn5Ni (at.%).

Solid-State Interfacial Reaction

The solid-state interfacial reactions of the Au-20wt.%Sn|Ni joints have been studied by aging samples at 150 °C [Wei13, Yoo07a, Yoo09], 200 °C [Son01, Wei13], 240 °C [Tsa05, Tsa06] and 250 °C [Yoo07a, Yoo09]. Even though, the experimental configurations vary with different literature, two common phe-nomena are presented: (i) the AuSn(Ni) adjacent to the interfacial reaction layer Ni3Sn2(Au) was replaced by Au5Sn [Son01, Tsa05, Tsa06, Yoo07a, Yoo09, Wei15]; and (ii) from 200 to 250 °C, the interfacial reaction layers consisted of: Au5Sn(Ni)/AuSn(Ni)/Ni3Sn2(Au) [Son01, Tsa06, Yoo07a, Yoo09, Wei15].

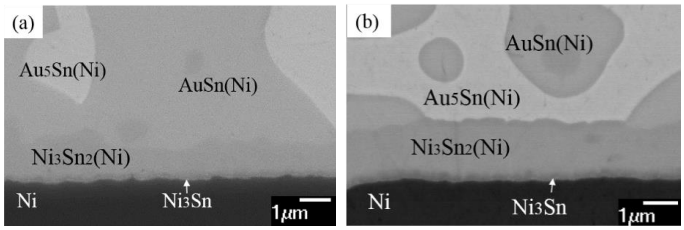

Figure 8. The SEM images of the subsequently aged Au-20wt.%Sn|Ni samples: (a) aged at 150 °C for 1200 h and (b) aged at 150 °C for 4600 h.

In the present study, the replacement of AuSn(Ni) by Au5Sn(Ni) on top of Ni3Sn2(Au) was also observed (Fig. 8). Besides, the thickness of Ni3Sn2(Au) was found growing linearly with the square root of increasing aging time. However, the precise composition of a slightly darker layer formed between Ni3Sn2(Au) and Ni could not be precisely identified by SEM/EDX due to the small thickness (Fig. 8(b)). Based on the calculated isothermal section of Au-Ni-Sn at 150 °C (Fig.9(a)), the formation of Au-rich phases (i.e. hcp, Au10Sn and fcc(Au)) at the Ni3Sn2(Au)/Ni interface cannot be excluded since Ni3Sn2(Au) can be in thermodynamical equilibrium with both Ni3Sn and these Au-rich phases without violating the mass-balance rule. However, the thin layer on top of Ni appeared slightly darker than (Ni1-x,Aux)3Sn2 (Fig. 8(b)), which implies that this layer contained more light elements than (Ni1-x,Aux)3Sn2. Therefore, it is reasonable to anticipate that Ni3Sn was formed at the (Ni1-x,Aux)3Sn2/Ni interface instead of these Au-rich phases.

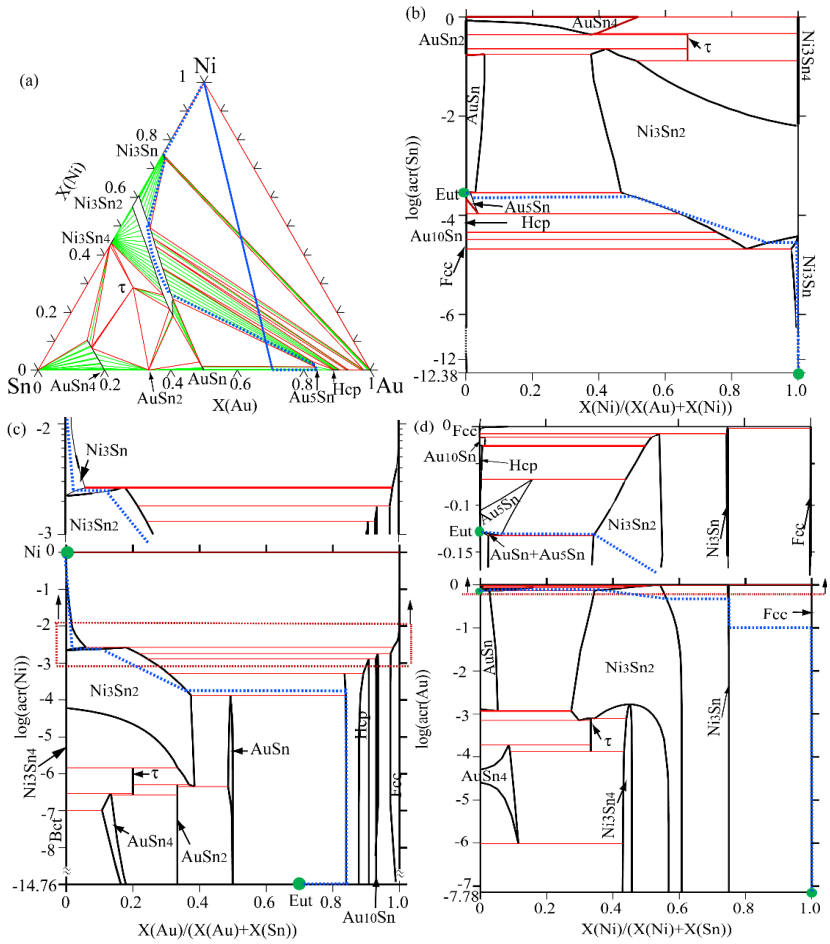

Figure 9. Calculations for the phase equilibrium of Au-20wt.%Sn|Ni at 150 °C: (a) the isothermal section of Au-Sn-Ni, the activity diagram of Sn (b), Ni (c) and (Au). Reference states: fcc(Au), fcc(Ni) and bct(Sn). The blue dotted-line is the proposed diffusion path of the reaction couple at 150 °C.

The calculated activity diagrams of species in Au-Ni-Sn system at 150 °C (Fig. 9(b) through (d)) can theoretically exclude the formations of these Au-rich phases at the (Ni1-x,Aux)3Sn2/Ni interface. As shown in the activity diagram of Au (Fig.9(d)), if any of the Au-rich in the Au-Ni-Sn ternary system were formed, the intrinsic diffusion of Au should then process towards the increasing of its activity. This is thermodynamically impossible [Loo90]. On the other hand, all of these species can intrinsically diffuse along the proposed sequence of the interfacial reaction layers (indicated by the dotted blue lines in Fig. 9(b) through (d)), which has been additionally supported by the calculated chemical potential of species along the proposed layer sequence (Table 6). Therefore, it is plausible to conclude: at 150 °C, the equilibrium diffusion path of Au-20wt.%Sn|Ni joints is: solder/Au5Sn(Ni)/Ni3Sn2(Au)/ Ni3Sn/Ni.

Table 6. The theoretically calculated chemical potential for each species at various interface of the diffusion couple. Reference states: Au(fcc), Ni(fcc) and Sn(bct).

Interface	Composition[C]		Chemical potential, J/mol		
	x(Au)	x(Ni)	Mur(Au)[M]	Mur(Ni)[M]	Mur(Sn)[M]
Eutectic/Au_5Sn	0.7071	2.6656E-4	-1053.3	-45145.9	-28601.3
Au_5Sn(Ni)/Ni_3Sn_2(Au)	0.2848	0.2498	-1062.2	-31154.8	-28829.1
Ni_3Sn_2(Au) /Ni_3Sn	7.7336E-2	0.5127	-1238.3	-20987.1	-37491.0
Ni_3Sn /Ni	4.3053E-6	0.7558	-8100.8	-2.6727E-2	-106287.1

[C] The compositions of the elements were selected from the tie-lines of the related two-phase fields, as was shown in Fig. 9(a). [M] Mur denotes the chemical potential of related elements.

5.1.2 Au-20wt.%Sn|Cu System

The equilibrium phase diagram of Au-Cu-Sn ternary system has been experimentally determined, including the pseudo-binary system AuCu-Sn and several isothermal sections at 170 °C [Roe88], 190 °C [Zak94], 200 °C [Yen07] and 360 °C [Kar92]. The entire phase equilibrium diagram has been thermodynamically established in a Master's thesis in 2007 [Sen07]. However, that set of thermodynamic parameters fails to describe the low temperature ordered-fcc phases, which have already been observed in both the Au-Cu binary system [Sun98] and the Au-Cu-Sn ternary system [Luc02]. In addition, the new thermodynamic properties of the Au-Cu-Sn liquid alloys have been experimentally measured by Knott et al. [Kno08], Wierzbicka-Miernik et al. [Wie10] and Guo et al. [Guo11] since 2008. Therefore, in this thesis the Au-Cu-Sn ternary system has been thermodynamically reassessed by considering the available thermodynamic properties of the ternary system [Kno08, Wie10, Guo11] and phase equilibria information [kar90, Kar92, Yen07]. The thermodynamic descriptions of the Au-Cu and Au-Sn binary systems have been taken directly from [Sun98] and [Don13]. Regarding the Cu-Sn system, the thermodynamic parameters of Cu41Sn11, Cu6Sn5_LT and Cu6Sn5_HT were reassessed in this work, and the thermodynamic parameters of the other phases in this system were adopted from [Li13]. In Publication II, a set of self-consistent thermodynamic parameters was presented.

Liquid/solid Interfacial Reaction.

The solid/liquid interfacial reactions of the Au-20wt.%Sn solder on Cu contact metallization was investigated by reflowing the samples at different temperatures, i.e. 290 °C [Tsa06], at maximum temperatures of 310 °C [So000] and 315 °C [Yoo7b], and 330 °C [Chu09] (listed in Table 7). The Au5Sn layer containing a large amount of Cu was observed at the interface. When extending the reflow periods from 100 s to a few minutes, both Chung et al. [Chu09] and Yoon et al. [Yoo07b] reported the formation of an AuCu layer at the Au5Sn(Cu)/Cu interface, and the coarse AuSn(Cu)+Au5Sn(Cu) two-phase areas formed in the solder matrix near the Au5Sn(Cu) layer. One special example is that Song et al. [Son00] observed a thin layer (≤ 0.5 μm, rich in Cu) at the Au5Sn(Cu)/Cu interface of the soldered Au-20wt.%Sn/Cu bump (280 ~315 °C for 75 s). However, only a single interfacial reaction layer of Au5Sn(Cu) was formed on the Cu/Au-20wt.%Sn/Cu solder joints (280 ~310 ° C for 10 min). They have attributed the observed different microstructures for the solder bump and the solder joint to the significantly slower cooling rate of the bonded solder joint than that of the solder bump [Son00].

In this study, the interfacial reaction product of Au5Sn(Cu) was observed as well (Fig. 10(a)). After soldering for 2500 s (Fig. 10(b)), we only detected the coarse AuSn(Cu)+Au5Sn(Cu) two-phase region at the solder/Au5Sn(Cu) interface. The AuCu layer at the Au5Sn(Cu)/Cu interface was not observed.

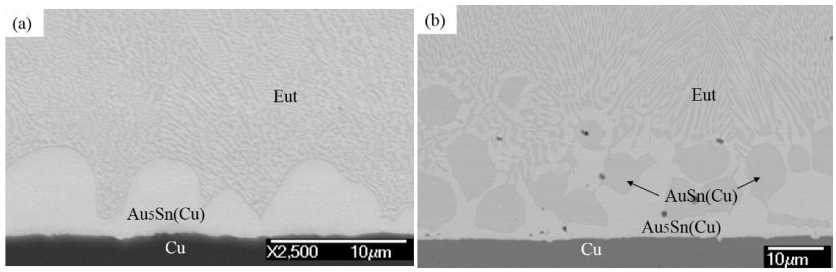

Figure 10. Cross-sectional SEM BSE images of the Au-20wt.%Sn|Cu joints soldered at 320 °C for: (a) 100s and (b) 2500 s.

The presence of AuSn(Cu)+Au5Sn(Cu) next to the interfacial reaction layer of Au5Sn(Cu) can be easily understood with the help of thermodynamic calculations (Fig. 11 (a) and (b)). When molten solder and Cu come in contact with each other, Cu starts to dissolve into the liquid immediately, meanwhile, Au and Sn atoms from the solder diffuse into Cu. The local nominal compositions of liquid and Cu vary along the contact line and move towards each other (Fig. 11(a)). When the composition of the liquid at the interface reaches the L+hcp(Cu) two phase field, the primary hcp(Cu) phase precipitates and grows at the interface. It acts as a barrier layer between the liquid and Cu. The continuous diffusion of Cu atoms into hcp(Cu) promotes the increasing of its thickness since hcp(Cu) can accumulate a significant amount of Cu (～28 and 47 at.% at 200 and 360 °C). Consequently, there will be a very limited amount of Cu dissolving into the residual liquid. This explains why the fine eutectic structure of Au-20wt.%Sn solder was formed on top of the Au5Sn(Cu) (Fig. 10(a)).

Table 7. Summary of Au-20wt.%Sn|Cu interfacial reactions investigations

Ref.	Sample	Thermal condition	Method	Statements
[Son00]	Z-MAJICTM bumped (diameter:140-145^{Uint}, tall: 55-65) Eut/(15-20) Cu	Bonding: 280-315 °C, 75 s	SEM-EDX	Overall composition of bulk solder: 60Au-10Cu-30Sn (atomic percent). Formation of a mushroom-shaped Au_5Sn(10-20Cu*) and a Cu-rich layer (<0.5 µm) at the interface.
		8 reflows, peak temperature 260 °C		Coarsening of eutectic structure: Au_5Sn(9-12Cu) and AuSn(<2Cu). At the interface: Au_5Sn(16-25Cu) layer decorated with AuSn precipitates/AuCu(7-8Sn).
		Aging: 200 °C, up to 80 d		Coarse eutectic lamellae: Au_5Sn(25-29Cu)+AuSn(~7Cu). At the interface: Au_5Sn(29Cu) with AuSn precipitates forming inside/AuCu (<1Sn)/ $AuCu_3$(2Sn) layers. AuCu and $AuCu_3$ layers had diffusion-controlled growth kinetics and thicken as t1/2.
	Z-MAJICTM bumped 5 Cu/ (diameter: 60, tall:25) Eut/5 Cu	Lamination reflow: 280-310 °C, 10 min		In the center: AuSn + Au_5Sn(19-22Cu) two phases. At both interfaces: thick Au_5Sn(29-31Cu) layer
		Aging: 150 °C, 20 d		Interface: (53-54)Cu-(41-42)Au-(5-6)Sn Cu-rich phase, thick Au_5Sn(23-27Cu) layer with AuSn precipitates scattered inside. In the middle: AuSn single phase
		Aging: 200 °C, 10, 20, 50 d		Dramatic change in phase distribution from 10 to 50 days aging, i.e. from 10-20 d of Cu/$AuCu_3$(2Sn)/AuCu/Au_5Sn(28-31Cu) decorated with AuSn precipitates/AuSn structure to 50 d of Cu/$AuCu_3$(2Sn)/AuCu(<1Sn)/(AuSn+AuCu+40Au40Cu20Sn three-phase region)/AuSn. Thickness of AuCu and $AuCu_3$ increase as t1/2.
		500 times thermal cycling: -65-150 °C		The thick Au_5Sn layer was replaced by multi-phases, with the overall composition of (46-56)Au(30-36)Cu(14-18)Sn. Crack formed at AuCu/multi-phases interface.
[Tsa06]	Evap. Multilayers:1.83 Sn/2.74 Au/ 5.8 Cu	290 °C, 2min	SEM, XRD, EPMA	Formation of Au_5Sn(17Cu) layer/AuSn(2.5Cu) +Au_5Sn(Ni) phases.
		240 °C, 2min		Formation of Au_5Sn(4.3Cu)/AuSn(1.5Cu) layers
		290 °C, 2 min, 240 °C 1, 10, 25 h		Microstructure changes with increasing annealing: 1 h, AuSn(3Cu)+Au_5Sn(Cu) phases/Au_5Sn(25-33Cu) layer, to 10 h, irregular layered AuSn(3Cu)/40Au40Cu20Sn/Au-Cu-Sn ternary compound with unknown composition/AuCu(Sn)/$AuCu_3$(Sn), and then to 25 h, Au6.6Cu9.6Sn3.8 layer/ Au-Cu-Sn ternary compound/AuCu(Sn)/$AuCu_3$(Sn).
		240 °C 2 min, 240 °C 1, 10, 25, 1000 h		Microstructure changes with increasing annealing: from AuSn(3Cu)/Au_5Sn(25-33Cu) to AuSn(3Cu)/40Au40Cu20Sn/Au-Cu-Sn/AuCu(Sn)/$AuCu_3$(Sn), to Au9.6Cu6.6Sn3.8 layer/ Au-Cu-Sn/AuCu(Sn)/$AuCu_3$(Sn), then to $Au_2Cu_6Sn_2$/AuCu(Sn)/$AuCu_3$(Sn)/Cu.

[Yoo07b]	Unknown thickness: Eut/Cu	Max. temperature 310 ºC, 60 s	SEM-EDX EPMA	Sample consists of: solder matrix/Au5Sn(17.6-32.7Cu) layer/Cu.
		Reflow: 310 ºC, 5, 15, 30, 60 min		No significant change in the interfacial microstructure. At solder/Cu interface: Au_5Sn(26.1-32.9Cu)/AuCu(7.5Sn) layers.
		Aging: 150 ºC, 100, 250, 500, 1000 h		Up to 500 hours, at solder/Cu interface: Au_5Sn(19.4Cu)/AuCu(1.9Sn) layers. Cu and Sn contents in hcp becomes rich with increasing aging time, from 19.4, 12.9 to 35.3 and 14.1 at.%. 1000 hours, AuCu(Sn) formed inside Au_5Sn(Cu)/irregular AuCu(Sn) layer.
		Aging: 250 ºC, 100, 250, 500, 1000 h		At solder/Cu interface: thick Au_5Sn(31.64Cu)/AuCu(0-2.9Sn)/$AuCu_3$(2.5Sn) layers. Crack formed inside AuCu(Sn) layer. Solder matrix: coursing with aging temperature.
[Chu09]	5400 Eut (prepared by melting pure Au and Sn shots)/254 Cu	Reflow: 330 ºC, 1, 5, 60 min	SEM EDX	Solder matrix: AuSn(2.74Cu)+ Au_5Sn(6.05Cu); At solder/Cu interface: Au_5Sn(19.36Cu)/ AuCu(6.8Sn). The Au_5Sn(Cu) had irregular interface. It grew in the form of pillars and extended into the solder matrix then formed the dendrites after reflowing for 60 min. The longer reflow time, the more coarse-eutectic-microstructures were formed.
		330 ºC 90 min, Cooled in furnace		Solder matrix: containing dendritic precipitates, some of them almost cross the solder matrix. At the solder/Cu interface, the irregular Au_5Sn(Cu) layer was formed.
		330 ºC 90 min, Fan cooling		Microstructure was similar to the sample cooled in furnace.
		330 ºC 90 min, Ice-quenching		Solder matrix: fine structure, without Au_5Sn(Cu) dendrite. Interface of Au_5Sn(Cu) layer was more uniform than the slower cooled sample.
	284 Eut/254 Cu	Reflow: 330 ºC, 1, 5, 60 min		The microstructure evolution was similar to the thicker sample, except for the tertiary arms were developed for some Au_5Sn(Cu) dendrites after reflowing for 60 min.
This work	100 Cu/100 Eut/100 Cu	Bonding: 320 °C 100 s	SEM EDX	Solder matrix: fine eutectic microstructure; At solder/Cu interface: Au_5Sn(13.5Cu) with a protruding scallop shape in the solder matrix.
		320 °C, 2500 sec		Fine solder/coarse AuSn(3.6Cu)+Au_5Sn(5.6Cu) phases/Au_5Sn(12.5Cu) layer/Cu.
		Aging: 150 °C, 1200, 2500, 4600, 6600 h		Solder: coarse eutectic structure; At the interface: Au_5Sn(Cu) became rich in Cu (up to 16 at.%) with AuSn(3.8Cu) precipitates dispersing inside/AuCu/$AuCu_3$ layers. $AuCu_3$ was formed after aging for 2500 hours. Thickness of AuCu and $AuCu_3$ grew with increasing aging time.
[Uint] The units for all layers are μm; * data shown in parentheses indicates the mole fraction of the dissolved third element; Eut means Au-20wt.%Sn solder.				

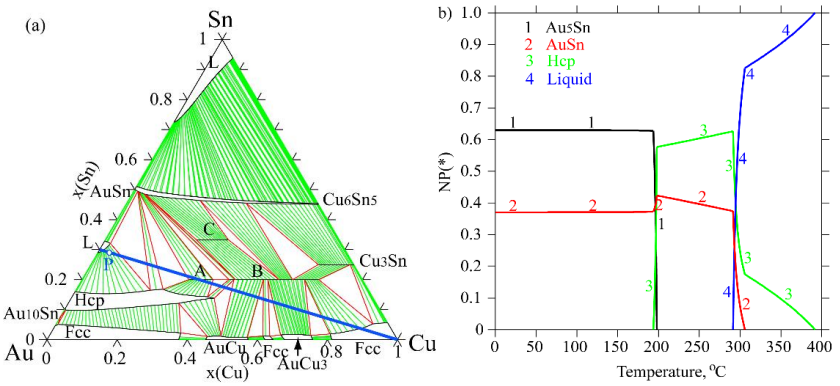

Figure 11. Calculated phase information: (a) isothermal section of Au-Cu-Sn at 320 °C; (b) the NP diagram showing the mole fraction of phases as functions of temperature with nominal composition of Au28.6at.%Sn4at.%Cu, marked with P in (a).

On the other hand, extending the soldering time results in increasing the content of Cu in the liquid until the saturation amount is reached. The solidification path of the liquid with the metastable solubility of Cu has been rationalized in Publication II based on the calculated graphs (Fig. 11).

Solid-State Interfacial Reaction

The solid-state interfacial reaction of the Au-20wt.%Sn|Cu metallization systems has been investigated by aging the samples at 150 °C [Soooo, Yoo07b], 200 °C [Soooo], 240 °C [Tsa06] and 250 °C [Yoo07b], as well as a reflow treatment to a peak temperature of 260 °C [Soooo] (summarized in Table 7). Overall, AuCu(Sn) and AuCu3(Sn) layers were formed next to the Cu substrate. In addition, the Au5Sn(Cu) layer formed during soldering was unstable, i.e. during aging, AuSn(Cu) particles were precipitated inside this layer.

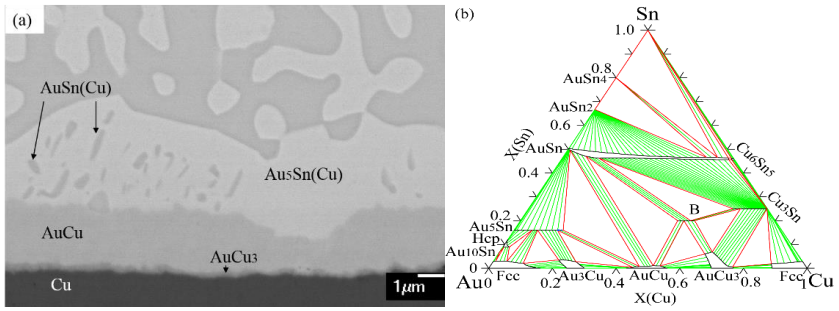

Figure 12. (a) microstructure of Au-20wt.%Sn|Cu after bonding at 320 °C for 100 s then aging at 150 °C for 6600 h. (b) the isothermal section of Au-Cu-Sn system at 150 °C.

The same phenomena have been observed in the present experimental work (Fig. 12(a)). The precipitation of AuSn(Cu) within Au5Sn(Cu) layer was attributed to the decomposition of hcp(Cu) formed during soldering, as shown in the calculated vertical section (Fig. 13). With regard to the sequence of the interfacial reaction layer, it can be rationalized with the method of thermodynamic calculation (See Publication IV). It was found that all the species in the

Au-20wt.%Sn|Cu metallization system at 150 °C can intrinsically diffuse along the diffusion path of solder/Au5Sn(Cu)/AuCu/AuCu3/Cu.

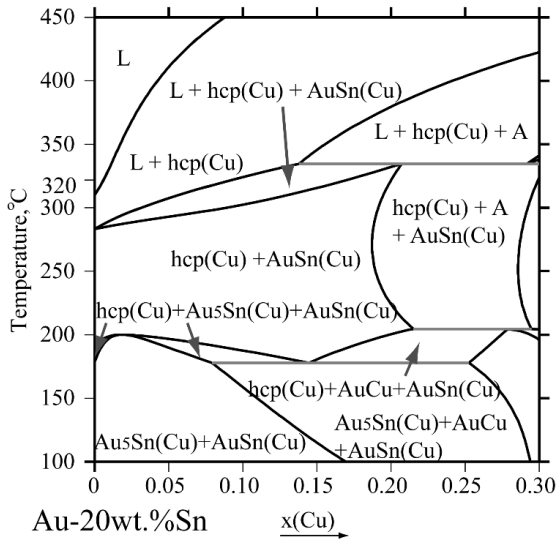

Figure 13. The calculated vertical section of (AuSn)eut-49.5Au20.5Sn30Cu (at.%).

5.1.3 Au-20wt.%Sn|Pt System

Before 2008, only two partial isothermal sections of the Au-Pt-Sn ternary system, i.e. at 400 °C [Tor01] and 25 °C [Anh98], had been reported. In order to acquire a realistic, consistent and reliable thermodynamic description of the Au-Pt-Sn ternary system, Grolier and Schmid-Fetzer experimentally investigated the phase equilibria in the range of Au-Pt binary edge to 40 at.% Sn [Gro08a]. Thermodynamic description of the Au-Pt-Sn ternary system was also presented in [Gro08a]. However, the revised lattice stability of Sn(hcp) was not used in [Gro08a]]. In order to be compatible with other Au-Sn-based higher-order multicomponent systems [Kro13], the Calphad approach was adopted in this thesis to acquire the self-consistent thermodynamic parameters of the Au-Pt-Sn ternary system (See Publication V). The reassessment of the Au-Pt-Sn ternary system was carried out based on the work of [Gro08a] by remodeling the AuSn, PtSn and the ternary phases as well as introducing the solubility of the third elements into binary compounds. For instance, the ternary interaction parameters of liquid were adopted from [Gro08a].The thermodynamic descriptions of the Au-Pt, Au-Sn and Pt-Sn binary systems were obtained from previous works [Xu12], [Don13] and [Gro08b], respectively.

A number of experimental investigations were implemented on the interaction of Au-Sn solder with Pt-based under-metallization at liquid state [Wad91a, Wad91b, Wad92, Kat92, Kat93, Kat94, Lee 92, Lee94, Kle97, Ive98, Pit01, Par02 and Gro08c] and solid state [Liu06 and Gro08c]. Table 8 lists the details of the experimental works of the Au-Sn|Pt-based system.

Table 8. Summary of Au-Sn/Pt interfacial reactions investigations

Ref.	Sample	Thermal condition	Method	Statements
[Wad91a] [Wad91b] [Wad92]	0.1^{Uint}Ti/0.3Pt/0.3-0.4Eut (thermal evap.)	Heating up to 400 °C	AES depth profile, SEM, XRD	Accumulation of Sn at the interface to react with Pt upon heating; With temperature increasing: forming increasing amount of PtSn at the interface and leaving pure Au layers. Interfacial reaction governed by the interdiffusion between solder and Pt.
[Kat92] [Kat93] [Kat94]	Thermal evap. 0.1Ti/0.2Pt/0.8Au/1.14Sn/0.8Au	320-350 °C, 5, 10 s	RBS, AES depth profile, SEM/EDX	After anneal at 320 °C for 10 seconds, formation of localized either Au-rich or Sn-rich areas in the solder and the very nonuniform of solder thickness across the pad. Within solder, existing empty spaces and gaps in several places. Sn tended to segregated towards Pt interface presumably forming Pt-Sn compounds.
	0.1Ti/0.2Pt/0.5Au/3 or 4x(0.35Sn/0.2Au)/0.5Au			After anneal at 320 °C for 10 seconds, the uniform thickness of Au-20wt.%Sn was formed on the pad. The overall thickness of solder for all of these three cases were around 2.7µm. Sn reacted with Pt to form the Pt-Sn compounds.
[Lee92]	e-beam evap. 0.1Ti/0.4Pt/3.2Au-Sn stack (64.4 at.% Au)	320 °C, 1 and 3 min	AES-depth profile	Prior to reflow: Au, Sn have intermixed completely with each other. During reflow, Pt reacted with Sn to form Pt-Sn compounds. The penetration depth of Sn into Pt layer was found to be 200 and 300 nm after 1 and 3 min of reflow.
[Kle97]	e-beam evap. 0.03Ti/0.3Pt/0.1Au/Eut	300 °C, to 10 min	SEM/EDX	After 30 s of reflow, Sn enrichment within the Pt layer to form Pt-Sn intermetallics. After 3 min of reflow: Pt barrier layer was consumed. 10 min: deep solder penetration into Si.
[Ive98]	0.025Ti/0.025Pt/0.25Au /1-3 Eut (e-beam evap. Au/thermal evap. Sn)	300 °C, 5 s	SEM/EDX, TEM/EDX	Pt dissolved into AuSn rather than Au_5Sn. A thin layer (~50nm) of Au_4Ti, dissolved some Sn, was formed between Ti and solder.
		265 °C, 5 s		Au layer incorporated in to the solder. Pt layer presented with some dissolved into the solder. Solder joints had uniform distribution of pores (diameter: < 1µm).
[Pit01]	Ti/Pt/3±0.5Au-Sn/Au/Pt	300-370 °C	SEM	Bulk solder: Using 0.1µm Au on the chip, it was eutectic composition; using 3µm Au on the chip, hcp phase was formed. At the interface: Pt layer was dissolved and reacted with Sn.
[Par02]	Pt/Eut	330 °C, to 4 h	SEM/EDX	Thickness of discontinuous interfacial reaction layer increased almost linearly with reflow time up to 7 min. The surface of Pt plat in contact with solder became roughened with the reflow progressing. Dissolution rate of Pt was ~0.6µm/min to 150 s of reflow, and become supersaturated at longer time.
	RF sputtering 0.1Ti/0.1Pt/0.1Au/Eut	330 °C, 3 min	SEM/EDX	Completely consumed Pt layer by dissolving into solder. A significant fraction of the interface was found to be debonded. Solder was in direct contact with Ti.
[Liu06]	0.02Ti/0.13Pt/2-3Au/5-6Eut	Reflow 315 °C	SEM/EDX	Sn from solder reacted with Au in Au layer.
		150 °C to 3 months		More Sn dissolved into Au layer to form Au-Sn compounds. No reaction between Pt and Sn observed.

[Gro08c]	e-beam evap. Ti/Pt/(4xAu/Sn), Au/Pt/Sn composition at.% of I:72/8/20 or II: 60/6/34	As deposited	XRD, SEM, GDOFS, TEM/EDX	Sn was consumed by reacting with Au to form AuSn. Bulk solder: AuSn+Au.
		180 °C, 2-32 min		Forming AuSn and Au_5Sn. No reaction involves Pt.
		230 °C, 10, 60 min		Sample I: for 10 min: reaction between Au and Sn to form AuSn + Au_5Sn and no reaction involving Pt; for 60 min, Sn from solder react with Pt- a ternary diffusion reaction.
		260 °C, 2-32 min		Sample I: quickly forming Au_5Sn and Sn from solder react with Pt- a ternary diffusion reaction. Sample II: for 32 min, detected three phases PtSn, AuSn, Au_5Sn.
		340 °C, 2-32 min		Sample I: formation of Au_5Sn/PtSn. Sample II: three phases PtSn, AuSn, Au_5Sn.
This work	Foils: 100Pt/100Eut/100Pt	320 °C, 100 s	SEM/EDX	Only forming $(Au_{1-x},Pt_x)Sn$ (with $0 \le x \le 0.5$) irregular layer (~0.7 µm thick), with AuSn binary alloy regions protruding into solder matrix. Here Pt content in $(Au_{1-x},Pt_x)Sn$ layer near Pt side was 9.1 at.%.
		Bonding 320 °C, 2500 s		Significant amount of Pt (i.e. 25 at.%) accumulated in the $(Au_{1-x},Pt_x)Sn$ intermetallic layer (~2.5µm thick), with irregular regions protruding deeper into solder matrix. Large isolated $(Au_{1-x},Pt_x)Sn$ areas were present in solder near interface. Roughen interface of IMC/Pt.
		Aging: 150 °C, to 4600 h		After 100 h, the average thickness of $(Au_{1-x},Pt_x)Sn$ layer have reached 3.3 µm, while remained constant with increasing aging time. The AuSn binary alloy areas were present in $(Au_{1-x},Pt_x)Sn$ layer till aged for 1200 h. After 2500 h, Pt contents was measured in solder matrix, 11 at.% in $(Au_{1-x},Pt_x)Sn$, and less than 2 at.% in Au_5Sn. In general, around ~22 at.% of Pt was measured in the $(Au_{1-x},Pt_x)Sn$ layer near Pt side; roughened interface of IMC/Pt was present; Within $(Au_{1-x},Pt_x)Sn$ layer, contrast was present in SEM graph, while no drastic composition difference was obtained via SEM/EDX analysis.
		320 °C, 100 s, 150 °C, 6864 h		Less irregular IMC/Pt interface compared with the other aging samples. Almost layered Au_5Sn(<0.5Pt*) phase formed at solder/$(Au_{1-x},Pt_x)Sn$ interface. Thinner $(Au_{1-x},Pt_x)Sn$ layer which dissolved up to 22 at.% Pt, was formed (~ 2.4 µm thick).
		320 °C, 500 s, 150 °C, 6864 h	SEM/EDX STEM/EDX	Voids and crack were present in $(Au_{1-x},Pt_x)Sn$ layer. Irregular interface of Pt in contact with IMCs. No Pt was detected in solder. Evidence of PtSn layer formed at $(Au_{1-x},Pt_x)Sn$/Pt interface. The average thickness $(Au_{1-x},Pt_x)Sn$ layer, was around 2.8 µm. AuSn binary alloy regions in $(Au_{1-x},Pt_x)Sn$ were observed via SETM with EDX.
Uint The units for all layers are µm; * data shown in parentheses indicates the mole fraction of the dissolved third element; Eut means Au-20wt.%Sn solder. GDOFS: glow discharge optical emission spectroscopy.				

However, those previous publications had different interpretations of the results. In particular, different interfacial reaction produces were reported, i.e. either forming Pt-Sn intermetallics [Wad91a, Wad91b, Wad92, Kat92, Kat93, Kat94, Lee92, Kle97] or Pt dissolving into solder [Ive98, Pit01, Par02] especially into the AuSn phase [Ive98]. Grolier and Schmic-Fetzer [Gro08c] claimed that the different experimental configurations could be attributed to the different interpretations in the literature published before 2008.

In order to understand the reaction phenomena of the bulk Au-20wt.%Sn|Pt interconnection, the present investigations were conducted. Two different soldering periods (i.e. 100 and 2500 s) were utilized to study the microstructural evolution of Au-20wt.%Sn|Pt during bonding at 320 °C. After 100 s of bonding, only one thin (~ 0.7 μm) and irregular interfacial reaction layer was observed from the cross-sectional SEM micrograph (Fig. 14(a)). Regions with markedly different compositions were measured by SEM/EDX analysis. The upper part of this layer (i.e. irregular areas protruding into the solder matrix) was composed of 50.5 at.% Au and 49.5 at.%Sn. At the lower part of this layer (i.e. next to Pt), high content of Pt was detected, for instance, near Pt, the composition of Au43.7Pt9.1Sn47.2 (at.%) was measured. The composition ratio of (Au+Pt) to Sn in both parts of this IMC layer is close to the stoichiometric ratio of 1:1, suggesting that this IMC layer was the AuSn-based intermetallic layer with Pt partially dissolved. As was reported [Tor01, Gro08a], at 400 °C, the solubility of Pt in AuSn was up to 25 at.% with constant Sn. Hereinafter, the phase notation of $(Au_{1-x},Pt_x)Sn$ (with $0 \le x \le 0.5$) was adopted to represent this intermetallic layer.

After 2500 s of bonding, the same intermetallic layer of $(Au_{1-x},Pt_x)Sn$ as observed in Fig. 14(a) was observed, while the maximum content of Pt was up to 25 at.% near the Pt layer (Fig. 14(b)) and the average thickness of the intermetallic layer has grew significantly (i.e. ~ 2.5 μm). In addition, Pt contents were measured in parts of the irregular region of the $(Au_{1-x},Pt_x)Sn$ IMC layer.

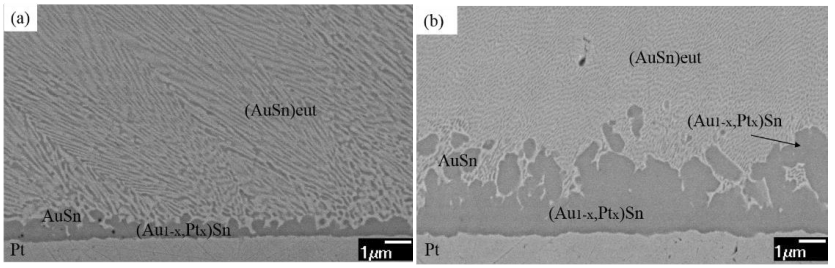

Figure 14. Cross-sectional SEM-BES images of as-soldered Au-20wt.%Sn|Pt samples after bonded at 320 °C for (a) 100 s and (b) 2500 s.

The microstructural evolution of Au-20wt.%Sn|Pt during soldering at 320 °C and the subsequent solidification were interpreted in Publication V with the help of thermodynamic consideration. The solubility of Pt in the molten solder is limited, i.e. less than 1 at.% according to [Gro08a]. The saturation of Pt in the liquid near the interface can be easily achieved in a short period, which promoted the rapid formation of $(Au_{1-x},Pt_x)Sn$ at the solder/Pt interface. Due to the significantly high solubility of Pt into AuSn (i.e. up to 25 at.% at 370 and 400 °C

[Gro08a, Tor01]), the formed $(Au_{1-x},Pt_x)Sn$ layer will prevent the further dissolution of Pt from the Pt substrate into the molten solder. Consequently, during solidification, the residual liquid will transform into the binary eutectic microstructure. The uneven thickness of the $(Au_{1-x},Pt_x)Sn$ layer could be attributed to the localized dissolution of Pt, as was estimated in [Par02].

Three groups of sandwich-like Pt/Au-20wt.%Sn/Pt samples were studied to reveal the solid-state interfacial reaction of Au-20wt.%Sn|Pt at 150 °C: (i) in group A, samples were bonded at 320 °C for 2500 s, then annealed at 150 °C for 100, 500, 1200, 2500, 4600 h; (ii) in group B, samples were bonded at 320 °C for 100 s, then annealed at 150 °C for 6848 h; and (iii) in group C, samples were bonded at 320 °C for 500 s, then annealed at 150 °C for 6848 h.

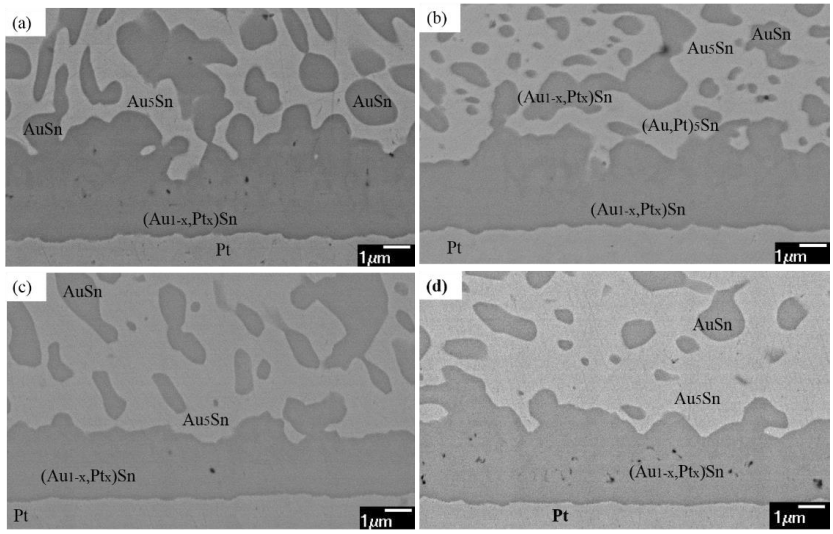

Figure 15. Cross-sectional SEM-BES images of aged Au-20wt.%Sn|Pt samples: bonded at 320 °C for 2500 s then aged at 150 °C for (a)100 h and (b) 4600 h; (c) bonded at 320 °C for 100 s then aged at 150 °C for 6848 h; and (d) bonded at 320 °C for 500 s then aged at 150 °C for 6848 h.

The representative cross-sectional SEM-BSE images of group A were shown in Fig. 15(a) and (b). The thickness of the interfacial reaction layer grew rapidly during the first 100 h of aging. Its average thickness reached 3.3 μm and remained constant during the extended aging period (i.e. up to 4600 h). The rapid growth of this IMC layer during a short aging time would have resulted from the filling of the gap between those protruded areas in the solder which were formed during soldering. When such protruded areas vanished, the growth of the IMC layer would be limited. The SEM/EDX analysis revealed that in the $(Au_{1-x},Pt_x)Sn$ layer the highest Pt content (up to 22 at.%) was obtained near the Pt layer. Besides, the existence of the AuSn binary compound areas in $(Au_{1-x},Pt_x)Sn$ was witnessed with EDX analysis until samples were aged for 1200 hours. The SEM-BSE image of sample aged for 4600 h (Fig. 15(b)) shows a slight contrast displayed in $(Au_{1-x},Pt_x)Sn$. However, no significant composition differences were obtained via SEM/EDX. Consequently, an analytical method with a higher resolution than SEM with EDX should be implemented.

In group B, the same interfacial reaction product (Fig. 15 (c)) was observed as that in group A. The largest Pt solubility (i.e. 22 at.%) in $(Au_{1-x},Pt_x)Sn$ was also detected at the area close to Pt. Besides, the IMC/Pt interface was more regular compared with those observed in group A.

In group C, the (Au1-x,Ptx)Sn intermetallic layer (~ 2.8 μm thick) was thicker than that formed in group B (~ 2.4 μm). The detail of the SEM-BES image shows that (Fig. 15(d)) almost layered Au5Sn was displayed on top of $(Au_{1-x},Pt_x)Sn$; In order to obtain a detailed microstructure of the interfacial reaction products, STEM with EDX was employed. Based on the STEM-HAAD image (Fig. 16(a)) and STEM/EDX results (Fig. 16(b) and (c)), the Pt solubility in $(Au_{1-x},Pt_x)Sn$ reached 25 at.% close to the Pt layer. Species that penetrated into the Pt layer was only Sn rather than both Sn and Au. The nano-scale PtSn layer was present at the $(Au_{1-x},Pt_x)Sn$/Pt interface. From the thermodynamic equilibrium viewpoint, the following local repartition next to Pt is conceivable: Au5Sn/$(Au_{1-x},Pt_x)Sn$/PtSn/Pt3Sn (See Publication V).

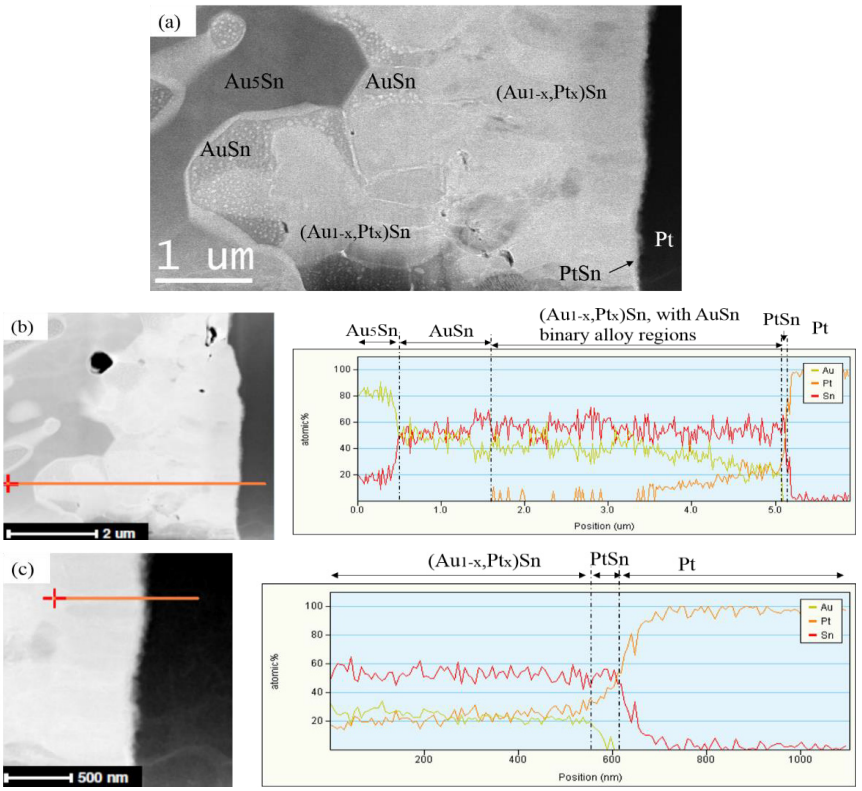

Figure 16. STEM-HAAD graph (a) and STEM/EDX profiles (b and c) of sample in group C.

5.2 Mechanical Properties

The advanced mechanical properties (such as the high creep resistance) of Au-20wt.%Sn solder promotes its utilizing in high temperature applications. Several experimental studies are readily available on the mechanical properties of

both individual AuSn and Au5Sn phases as well as the eutectic composition alloy itself [Ciu89, Yos90, Vic04, Chr05, Wan14]. Ciulik and Notis measured the microhardness of AuSn and Au5Sn using a microhardness tester with a load of 50 gram [Ciu89]. Yost et al. measured the elastic properties of AuSn, Au5Sn and the eutectic alloy (i.e. poisson's ratio, bulk modulus, Young's modulus and shear modulus) in a temperature range of 25 to 250 °C by resonance techniques [Yos90]. Vicenao et al. implemented microindentation measurements on the electroplated Au-Sn alloys to study the Vickers microhardness and elastic modulus of fcc-Au(Sn), hcp-AuSn and δ-AuSn [Vic04]. Chromik et al. systematically investigated the hardness and elastic modulus of intermetallic compounds and the Au-20wt.%Sn eutectic alloy in the Au-Sn system by nanoindentation. In addition, they found that Au5Sn, Au-20wt.%Sn alloy and AuSn were significantly more creep resistant than common soft solders by performing the indentation creep measurements on these alloys [Chr05]. Recently, Wang et al. studied the indentation size effect and micromechanics characterization of intermetallics in the Au-Sn system. They reported that the creep of AuSn and Au5Sn were dominated by dislocation viscous glide and grain boundary sliding respectively, by employing a viscoplastic creep equation to evaluate the creep behavior of the Au-Sn intermetallics [Wan14]. In the present study, the hardness and elastic modulus of AuSn and Au5Sn were measured by nanoindentation tests. A fair agreement was achieved between our results and data reported in previous experimental investigations (Publication III).

The mechanical properties of the Au-20wt.%Sn|X (X=Ni, Cu and Pt) solder joints have rarely been measured, except for two studies on Au-20wt.%Sn|Ni metallization system. Wei et al. [Wei13] and Yoon et al. [Yoo07a] conducted shear tests on the aged samples where data obtained from the as-reflowed joints were treated as the starting points. However, contradictory results were reported. For instance, Yoon et al. observed that the shear force decreased only at the initial 100 h at 150 °C or 250 h at 250 °C, and then remained nearly constant with prolonged aging [Yoo07a]. The results from [Wei13] indicated a slight decrease of shear strength at 150 °C and the drastic decrease of shear strength at 200 °C. In addition, the failure modes proposed by them were conflict, i.e. at 150 °C, Wei et al. observed the fracture at the solder/IMC interface rather than through the bulk solder as stated by Yoon et al. [Yoo07a]. Studying the reliability of the TiW/Ni/Au/Sn (with composition of 82.7 at.%Au-17.3 at.% Sn) TLP bonding samples, Xu et al. [Xu14] and Rautiainen et al. [Rau15] reported that the failures were mainly along the Ni3Sn2(Au)/Ti interface. So far no literature is available with regard to the mechanical properties of the individual interfacial reaction products formed in the Au-20wt.%Sn|X (X=Ni, Cu and Pt) systems. In this thesis, nanoindentation measurements were implemented on the interfacial reaction products formed at the Au-20wt.%Sn/Ni and Au-20wt.%Sn/Cu interfaces.

Regarding the Au-20wt.%Sn|Ni aged samples, indents were located in the phase regions of AuSn(Ni), Au5Sn(Ni) and Ni3Sn2(Au). The hardness and indentation modulus of these alloys were deduced from the collected

load displacement curves (or called *P-h* curve). Based on the deduced results, it was evidenced that the solubility of the third element influenced markedly on the hard-ness and indentation modulus of the respective compounds, i.e. the mechanical property values of AuSn(Ni) and Au5Sn(Ni) increased with the increasing con-tent of the dissolved Ni, while those of Ni3Sn2(Au) changed in the opposite way. When studying the compounds formed at the solder/Cu interface, we obtained the hardness and indentation modulus of AuSn(Cu), Au5Sn(Cu) and AuCu al-loys. In addition, the similar influence of Cu on the mechanical properties of AuSn(Cu) and Au5Sn(Cu) were obtained. Specifically, when dissolving more Cu, AuSn(Cu)and Au5Sn(Cu) would have higher values of hardness and indentation modulus. Moreover, in both of these system, the 'pop-in' phenomena were ob-served on the *P-h* curve of Ni3Sn2(Au), Au5Sn, Au5Sn(Ni) and Au5Sn(Cu) (Fig. 17). We attempted to ascribe such 'pop-in' phenomena to the load-induced dis-location activities due to volume shrinkage-induced micro-defects [Yos90] (Publications III and IV). However, no further evidence can support the inter-pretation of the 'pop-in' events observed in this work. Thus, more investigations are required before the mechanism of the related phenomenon can be unambig-uously rationalized. The present measurements indicated that Ni3Sn2(Au) and AuCu had the relatively high hardness and poor ductility in their respective sys-tems. When the interconnections were subjected to high external stress loading and strain rate, the stress concentration adjacent to Ni3Sn2(Au) and AuCu would cause fractures along the interfaces.

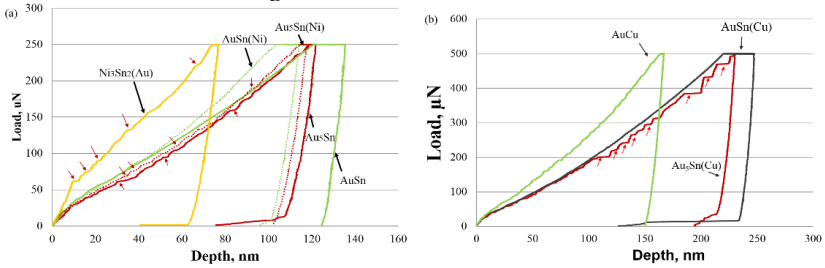

Figure 17. Load versus displacement curves for nanoindentation testing implemented on (a) the Au-20wt.%Sn|Ni samples and (b) the Au-20wt.%Sn|Cu samples. Some of the 'pop-in' events are indicated by red arrows in each case.

5.3 Comparisons among Au-20wt.%Sn|X (X=Ni, Cu, Pt)

The applicability of the Au-20wt.%Sn/Pt/Ti bonding scheme in optoelectronic applications had been widely accepted [Wad91a, Wad91b, Wad92, Kat93, Kle97] till the concern arose on the rapid consumption of the Pt barrier layer at high temperature (300-350 °C) [Kat92]. Lee et al. [Lee92, Lee 94] and Katz et al. [Kat 94] proposed the replacement of Pt(400 nm)/Ti metallization by Ni(300 nm)/Ti. They claimed that more Sn was consumed by Pt than by Ni since after 3 min of reflow, 250 nm of Ni and 300 nm of Pt have reacted with Sn. However, those intact areas by Sn were either Pt-Ti or Ni-Ti mixture regions. Based on those reports, one could not unambiguously anticipate that the reaction be-tween Pt and Au-20wt.%Sn solder was faster than that observed at the Ni/solder

interface without excluding the influence of Ti. In 2002, Park et al. detected a thicker interfacial reaction layer at the solder/Ni interface than that formed at the solder/Pt interface by reflowing Au-20wt.%Sn/(Ni or Pt) samples at 330 °C for up to 3 min [Par02]. In this thesis, when samples were soldered at 320 °C for 100 s the same result as reported in [Par02] was obtained, i.e. a thinner intermetallic layer was observed at the Au-20wt.%Sn/Pt interface than that formed at the Au-20wt.%Sn/Ni interface. When samples were bonded at 320 °C for 2500 s, on the contrary, the thicker IMCs was formed in the solder/Pt system than that in the solder/Ni system. Nevertheless, as reported by Katz et al. the efficient bonds were achieved with only keeping the molten Au-20wt.%Sn solder (at 300-350 °C) on top of Ti/Pt for 6 seconds [Kat93].

At liquid state, Cu dissolves faster into molten solder than Ni and Pt to form a thick interfacial reaction layer at the solder/Cu interface. Provided that the met-allurgical bond between Cu and Au-20wt.%Sn solder can be achieved, an addi-tional diffusion barrier has to be placed between Au-20wt.%Sn solder and Cu to prevent the fast interfacial reaction since rapid consumption of solder will de-grade the self-assembly behavior of the molten solder.

Tsai et al. compared the microstructure evolution of Au/Sn (with composition of Au-20wt.%Sn) on Cu and Ni substrates at 290 and 240 °C [Tsa06]. They concluded that the thermal stability of Au20wt.%Sn|Ni was better than that of Au20wt.%Sn|Cu. However, a change in the layer sequence was observed at the aged Au-20wt.%Sn/Ni interface in this thesis and by other researchers [Son01, Tsa05, Tsa06, Yoo07a, Yoo09, Wei15], namely, the adjacent of AuSn(Ni)/Ni3Sn2(Au) was gradually replaced by Au5Sn(Ni)/Ni3Sn2(Au) when the aging process were progressed. In the Au-20wt.%|Cu system, similar microstructures were observed during aging except for the growth of AuCu and AuCu3 layers. Even though, these results suggest that at 150 °C the Au-20wt.%Sn|Cu joints are more thermally stable than Au-20wt.%Sn|Ni, cracks were observed in solder/Cu interconnections in this study as reported by Song et al. [Son00] and Yoon et al [Yo07a].

On the other hand, the solid-state interfacial reactions of Au-20wt.%Sn solder on Ni and Cu were more complex than that of Au-20wt.%Sn|Pt. In the former two systems, all species in the respective metallization systems participated in the interfacial reactions resulting in the formation of several interfacial reaction products within a short period of aging. The diffusion controlled growth of interfacial reaction products at 150 °C was witnessed in both Au-20wt.%Sn|Ni and Au-20wt.%Sn|Cu systems. Nevertheless, the interfacial reaction of Au-20wt.%Sn solder on Pt, was comparatively simple with a constant thickness of the interfacial reaction product during a long period of aging (from 100 to 4600 h). The excessive growth of the IMC layer might be detrimental to the reliability of the solder joints due to the brittle natures of these IMCs and the physical properties mismatch [Lee07]. Therefore, one could expect that Au-20wt.%Sn|Pt interconnections have better thermal stability than both Au-20wt.%Sn|Ni and Au-20wt.%Sn|Cu at 150 °C.

However, even though the Au-20wt.%Sn|Pt metallization system can provide a good bond when the soldering time is short (e.g. less than 1 minute at 300 °C

for a 300-nm-thick Pt barrier layer [Kle97]), the excessive reaction between AuSn and Pt to form (Au1-x,Ptx)Sn in a long soldering duration would degrade the barrier behavior of Pt and the self-alignment of the molten eutectic solder thus resulting in delamination of the metal and failure of the bond [Kat94]. For these reasons, care must be taken, especially in the TLP bonding process where the bonding periods are always in tens of minutes. The solution in general includes: (i) adjusting the Pt thickness [Par02] and (ii) employing a multi-layered metallization scheme (e.g. Ti/Pt/Au in [Pit01]). When defining the thickness of the barrier layer, one must take into account the soldering parameters (such as, the bonding temperature and time) and the solder joint thickness requirement [McN08]. On the other hand, if neither of these methods works, the replacement of Pt [Lee92, Kat92, Kat94, Par02] can be the alternative solution. W, Cr, Co and Rh were suggested as the alternatives to the Pt barrier layer [Wad91b, Wad92, Kat92, Liu06, Par02]. However, an inert barrier layer (e.g. Cr, W) has a tendency to cause dewetting [Kat94, Lee94, Kle97]. In addition, few investigations are available on Au-20wt.%Sn|Co and Au-20wt.%Sn|Rh metallization. Specifically, only the dissolution rate of Co into Au-Sn molten solder during reflow [par02] and the diffusion coefficient and activation energy for Rh [Wad92] were reported. Consequently, even though novel information of Au-20wt.%Sn|X metallizations is obtained in this thesis, some issues still remain open for further investigation.

6. Summary

The eutectic alloy of Au-20wt.%Sn has received considerable attentions: (i) as available alternative to high-temperature high-lead die attach material for power semiconductors, and (ii) the wafer-level bonding material for MEMS packaging. In order to design the reliable contact metallization for Au-20wt.%Sn solder, phase diagrams of Au-Sn-X (Ni, Cu and Pt) were established based on the Calphad approach. The principle of the diffusion couple method was adopted to acquire the microstructure of the as-soldered and subsequently aged Au-20wt.%Sn/X samples. The interfacial reaction of the as-soldered (at 320 °C) and subsequently aged Au-20wt.%Sn|X interconnections have been investigated.. Furthermore, by implementing the nanoindentation tests, the mechanical properties (i.e. hardness and elastic modulus) of the IMCs formed at the Au-20wt.%Sn/Ni and Au-20wt.%Sn/Cu interfaces have been extrapolated from the collected load-displacement curves. The calculated phase diagrams indicate these three metallization systems are complex. Nevertheless, the interfacial reaction of Au-20wt.%Sn solder on the these selected contact metallizations can be efficiently interpreted by combining experimental investigations and basic thermodynamic considerations. Results from nanoindentation measurements indicate the solubility of the third elements have significant influences on the hardness and modulus of the individual IMCs. This has been induced by the replacement of the soft and less stiff Au by Ni or Cu, and vice versa.

Based on the result of this dissertation, we concluded that during a short bonding period (i.e. 100 s) at 320 °C, less Pt layer will be consumed by reacting with Au-20wt.%Sn solder than Ni and Cu. However, Ni is superior to Pt and Cu as a barrier layer when subjected to a long bonding period at 320 °C (i.e. 2500 s). Cu has the most rapid dissolution rate among these three contact metallizations. It suggests that a good metallurgical bond can be obtained between solder and Cu, however, a diffusion barrier layer must be placed between Au-20wt.%Sn solder and Cu layer to avoid the rapid consumption of the contact metallization. At the solid-state, Au-20wt.%Sn|Pt shows better thermal stability than the other two.

The main results of the five appended publications are summarized as follows:

Publication I, entitled “Thermodynamic reassessment of Au-Ni-Sn ternary system”, presented (i) details of thermodynamic models adopted to reassess the Au-Ni-Sn ternary system, (ii) a self-consistent set of thermodynamic parameters of this system, as well as (iii) the microstructure of the Au-20wt.%Sn|Ni interconnection during bonding and aging. The liquidus projection and the ternary invariant reaction involving liquid phases have been extrapolated by using the acquired thermodynamic parameters. Based on the experimental results, a diffusion path at 150 °C was proposed on the calculated isothermal section.

Publication II, entitled “Thermodynamic reassessment of Au-Cu-Sn ternary system”, introduced the application of a four-sublattice-site to model the disorder-order transitions of fcc-phases. A set of thermodynamic parameters was acquired to thermodynamically describe Au-Cu-Sn. A fair agreement was achieved between the calculated data and the experimentally measured values. SEM and SEM/EDX analysis were employed to characterize the microstructures of the soldered and aged Au-20wt.%Sn|Cu reaction couples. A phase friction diagram (or called as NP diagram) was calculated to rationalize the solidification sequence of molten solder close to the original solder/Cu interface.

In publication III, entitled “Microstructural evolution and mechanical properties of Au-20wt.%Sn|Ni interconnection”, interfacial reaction of Au-20wt.%Sn on Ni at 320 and 150 °C were experimentally investigated. A diffusion controlled growth of Ni3Sn2(Au) was observed. The reaction phenomena in as-soldered and aged Au-20wt.%Sn|Cu samples were interpreted by combining the experimental results with thermodynamic considerations. A plausible diffusion path was proposed based on calculated phase diagrams (i.e. isothermal section and activity diagrams) and thermodynamic properties as well as the experimental results. At 150 °C, the sequence of the reaction layers at the Au-20wt.%Sn/Cu interface consisted of Au5Sn(Ni)/Ni3Sn2(Au)/Ni3Sn instead of AuSn(Ni)/Ni3Sn2(Au)/Ni3Sn which was proposed in Publication I. Moreover, nanoindentation measurements were implemented to collect the mechanical properties of interfacial reaction products formed at the Au-20wt.%Sn|Ni interface. It was found that the dissolution of a third element significantly affected the mechanical properties of those IMCs, i.e. the higher Ni solubility, the larger hardness and indentation modulus values of AuSn(Ni) and Au5Sn(Ni) were measured, while the solubility of Au in Ni3Sn2(Au) had an opposite influence on its hardness and indentation modulus. The ‘pop-in’ phenomena were observed in the load-displacement curves of Ni3Sn2(Au), Au5Sn and Au5Sn(Ni). It would be ascribed to the pre-existing micro-defects resulted from the volume shrinkage during hcp→Au5Sn phase transformation. On the basis of the microstructural characteristic and mechanical properties of the IMCs in the Au-20wt.%Sn/Ni interface, the potential reliability risks of this interconnection was addressed. If the solder joint was subjected to high external loading and a high strain rate, the interfaces of Ni3Sn2(Au) might be the weak part of the joint due to the growth of Ni3Sn2(Au) with a prolonged aging process and its relatively

high hardness and modulus. Besides failure might occur inside of the Au5Sn(Ni) layer due to the accumulation of pre-existing microdefects.

In publication IV, entitled “Microstructural evolution and mechanical properties in (AuSn)eut-Cu interconnections”, the same methodologies as in Publication III were employed to (i) reveal the microstructural characterization of as-soldered and aged Au-20wt.%Sn|Cu reaction couples, (ii) interpret the observed reaction phenomena, (iii) rationalize the sequence of interfacial reaction at 150 °C, as well as the mechanical properties of individual reaction products. At 150 °C, the sequence of interfacial reaction layers at the Au-20wt.%Sn/Cu interface was: Au5Sn(Cu)/AuCu/AuCu3. Pop-in phenomena were observed in the P-h curve of Au5Sn(Cu) as well. The dissolving of Cu in AuSn(Cu) and Au5Sn(Cu) resulted in the increasing of their hardness and modulus values. However, AuCu still had the highest values of hardness and indentation modulus.

Publication V, entitled “Thermodynamic reassessment of the Au-Pt-Sn ternary system and microstructural evolution of (AuSn)eut-Pt interconnection”, provided the thermodynamic descriptions of the Au-Pt-Sn system by considering available thermodynamic properties and phase equilibria information. Microstructure of as-solder and as-aged Au-20wt.%Sn|Pt reaction couples were characterized by analyzing three sets of samples with the methods of SEM with EDX and STEM with EDX. At the liquid-state, the interfacial reaction did not follow the diffusive-reaction mechanism. At solid state, the observed thickness of the IMC layer was barely changed from 100 to 4600 h of aging at 150 °C. STEM results showed that (i) the AuSn binary alloy regions were displayed in the $(Au_{1-x},Pt_x)Sn$ (with $0 \le x \le 0.5$) layer; and (ii) a very thin PtSn layer was formed at the $(Au_{1-x},Pt_x)Sn$/Pt interface. In addition, in one sample cracks and voids were presented in the $(Au_{1-x},Pt_x)Sn$ intermetallic layer. Based on the thermodynamic equilibrium and experimental results, the equilibrium reaction sequence of Au-20wt.%Sn|Pt at 150 °C would eventually consists of: Au5Sn/$(Au_{1-x},Pt_x)Sn$/PtSn/Pt3Sn. The advantages and disadvantages of Au-20wt.%Sn|X (X=Ni, Cu and Pt) were compared.

References

[Abt00] Abtew M., Selvaduray G., "Lead-free solders in microelectronics," *Materials Science and Engineering: R: Reports*, 2000, 27(5): 95-141.

[Ågr96] Ågren J., "Calculation of phase diagrams: Calphad," *Current Opinion in Solid State and Materials Science*, 1996, 1(3): 355-360.

[Ant11] Anthony C., Fischer-Cripps A.C., "Nanoindentation testing," *in Nanoindentation, 3rd edition,* 2011, Springer, New York, pp. 21-37.

[Bak92] Baker H., "Introduction to alloy phase diagrams," *in ASM Handbook Vol. 3: Alloy Phase Diagrams*, 1992, ASM international, Materials Park, OH, pp. 1-30.

[Bra08] Brandon D., Kaplan W.D., "The concept of Microstructure," *in Microstructural Characterization of Materials, 2nd edition,* 2008, John Wiley & Sons Ltd, pp. 1-54.

[Ber15] Berger D., Nissen J., "Measurements of the quantitative lateral analytical resolution at sputtered gold-layers with the FEG-EPMA JEOL JXA-8530F," *IOP Conference Series: Materials Science and Engineering*, 2016, 109(1): 012001.

[Bul75] Bulychev S.I., Alekhin V.P., Shorshorov M.H., Ternovskii A.P., Shnyrev G.D., "Determining Young's modulus from the indentor penetration diagram," *Zavodskaya Laboratoriya*, 1975, 41(9): 1409-1412.

[Cam12] Campbell F.C., "Phase diagram determination," *in Campbell F. C. (ed.), Phase Diagrams: Understanding the Basics*, 2012, ASM International, pp. 239-262.

[Cho10] Chorfa A., Madjoubi M.A., Hamidouche M., Bouras N., Rubio J., Rubio F., "Glass hardness and elastic modulus determination by nanoindentation using displacement and energy methods," *Ceramics-Silikáty*, 2010, 54(3), 225-234.

[Chr05] Chromik R.R., Wang D.N., Shugar A., Limata L., Notis M.R., Vinci R.P., "Mechanical properties of intermetallic compounds in the Au–Sn system," *Journal of Materials Research*, 2005, 20(08): 2161-2172.

[Chi10] Chin H.S., Cheong K.Y., Ismail A.B., "A review on die attach materials for SiC-based high-temperature power devices," *Metallurgical and Materials Transactions B*, 2010, 41(4): 824-832.

[Chi11] Chidambaram V., Hattel J., Hald J., "High-temperature lead-free solder alternatives," *Microelectronic Engineering*, 2011, 88(6): 981-989.

[Chu09] Chung H., Chen C., Lin C., Chen C., "Microstructural evolution of the Au–20wt.% Sn solder on the Cu substrate during reflow," *Journal of Alloys and Compounds*, 2009, 485(1): 219-224.

[Ciu89] Ciulik J, Notis M.R., "Phase Equilibria and Physical Properties in the Au--Sn System," *Microelectronic Packaging Technology: Materials and Processes* (Retroactive Coverage), 1989: 57-61.

[Cop07] Coppola L., Huff D., Wang F., Burgos R., Boroyevich D., "Survey on high-temperature packaging materials for SiC-based power electronics modules," *Power Electronics Specialists Conference, IEEE*, 2007: 2234-2240.

[Dęb10] Dębski A., Gąsior W., Moser Z., Major R., "Enthalpy of formation of intermetallic phases from the Au–Sn system," *Journal of Alloys and Compounds*, 2010, 491(1): 173-177.

[Din91] Dinsdale A.T., "SGTE data for pure elements," *Calphad*, 1991, 15(4): 317-425.

[Don13] Dong H.Q., Tao X.M., Laurila T., Vuorinen V., Paulasto-Kröckel M., "Thermodynamic modeling of Au–Ce–Sn ternary system," *Calphad,* 2013, 42: 38-50.

[Eil15] Eilken B., "DA5 customer presentation," available online: http://www.infineon.com/dgdl/DA5_customer_presenttion.pdf?fileId=db3a30433fa9412f013fbd2aed4779a2.

[Esa08] Esashi M., "Wafer level packaging of MEMS," *Journal of Micromechanics and Microengineering*, 2008, 18(7): 073001.

[EUR] EU law and Publication, Available online: http://eur-lex.europa.eu/legal-content/EN/TXT/?uri=CELEX%3A32002L0095

[Exn96] Exner H.E., "Qualitative and quantitative surface microscopy," *in Cahn R.W., and Haasen P. (eds.) Physical metallurgy, 4th edition,* 1996, Elsevier Science, The Netherland, pp. 943-1032.

[Exn04] Exner H.E., Weinbruch S., "Scanning Electron Microscopy," *in Vander Voort G.F. (ed.), Metallography and Microstructures*, Vol. 9: ASM Handbook, 2004, ASM International, pp. 355–367.

[Far14] Farrens S., Sood S., MicroTec S., "Wafer level packaging: Balancing device requirements and materials properties," *Proceeding of Pan Pacific Microelectronics Symposium conference,* 2014: 22-24.

[Gar15] Garnier A, Baillin X, Hodaj F., "Interfacial reactions and diffusion path in gold–tin–nickel system during eutectic or thermo-compression bonding for 200 mm MEMS wafer level hermetic packaging," *Journal of Materials Science: Materials in Electronics*, 2015, 26(6): 3427-3439.

[Giu13] Giudice S., Bosshard C., "Au-Sn Transient Liquid Phase bonding for hermetic sealing and getter activation," *Microelectronics Packaging Conference (EMPC), IEEE*, 2013: 1-5.

[Gok75] Gokcen N.A., "Standard Gibbs energy change of reactions," *in Thermodynamics,* 1975, United States of America: Parker & Sons, pp. 281-335.

[Gro08a] Grolier V., Schmid-Fetzer R., "Experimental Study of Au-Pt-Sn Phase Equilibria and Thermodynamic Assessment of the Au-Pt and Au-Pt-Sn Systems," *Journal of Electronic Materials*, 2008, 37(3): 264-278.

[Gro08b] Grolier V., Schmid-Fetzer R., "Thermodynamic analysis of the Pt–Sn system," *Journal of Alloys and Compounds*, 2008, 450(1): 264-271.

[Gro08c] Grolier V., Schmid-Fetzer R., "Diffusion-Reaction in the Au-Rich Ternary Au-Pt-Sn System as a Basis for Ternary Diffusion Soldering," *Journal of Electronic Materials*, 2008, 37(6): 815-828.

[Guo11] Guo Z., Hindler M., Yuan W., Mikula A., "Thermodynamic properties of liquid Au–Cu–Sn alloys determined from electromotive force measurements," *Thermochimica Acta*, 2011, 525(1): 183-189.

[Hao15] Haond M., "Fully depleted SOI: Achievements and future developments," *Ultimate Integration on Silicon (EUROSOI-ULIS), 2015 Joint International EUROSOI Workshop and International Conference on, IEEE*, 2015: 37-40.

[Har09] Hartnett A., Buerki S., "Process and reliability advantages of AuSn eutectic die attach," *Proceeding of 42nd International Symposium on Microelectronics*, 2009: 281-287.

[Has08] Hashimoto S., Sakurada T., Suzuki M., "Lateral Resolution of EDX Analysis with Low Acceleration Voltage SEM," *Journal of Surface Analysis*, 2008, 14(4): 428-432.

[Hil80] Hillert M., "Empirical methods of predicting and representing thermodynamic properties of ternary solution phases," *Calphad*, 1980, 4(1): 1-12.

Aalto-DD 176/2016

ISBN 978-952-60-6996-8 (printed)
ISBN 978-952-60-6995-1 (pdf)
ISSN-L 1799-4934
ISSN 1799-4934 (printed)
ISSN 1799-4942 (pdf)

Aalto University
School of Electrical Engineering
Department of Electrical Engineering and Automation
www.aalto.fi

BUSINESS + ECONOMY

ART + DESIGN + ARCHITECTURE

SCIENCE + TECHNOLOGY

CROSSOVER

DOCTORAL DISSERTATIONS